Electronics World

www.electronicsworld.co.uk

February 2019
Volume 125
Issue 1990
£5.90

In this issue...

Design of analogue, digital, transformer and RF systems

also ...

Cabling and the invisible threat of non-compliance

Industrial IoT systems

need high integration and small form factor power conversion

Discover Your Power

Flexibility to Choose the Desired Power Solution

As a leading supplier with a comprehensive power management and monitoring portfolio, Microchip gives you the power, flexibility and confidence to choose the right solution for your design.

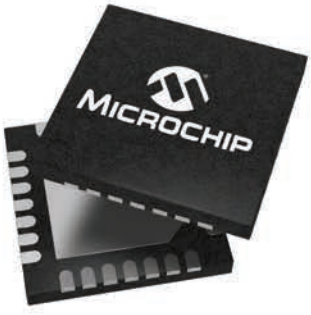

Managing your system's power usage is crucial to achieving the performance that your design requires. Our product portfolio of power monitoring devices allows you to accurately measure active, reactive and apparent power, Root Mean Square (RMS) current and voltage, line frequency, and power factor. Our broad selection of power management devices including DC-DC controllers and regulators, MOSFETs and MOSFET drivers, voltage supervisors and references, and power modules enables you to efficiently design a solution to manage the power requirements of your system.

From reference designs to evaluation boards to simulation tools, you'll reduce design-in time and minimize risk with the comprehensive support Microchip can offer.

Discover your power at
www.microchip.com/PowerSolutions

MICROCHIP

Electronics World

February 2019

EDITOR:
Svetlana Josifovska
Tel: +44 (0)1732 883392
Email: svetlanaj@electronicsworld.co.uk

SALES:
Suzie Pipe
Tel: +44 (0)20 8306 0564
Mobile: +44 (0)7799 063311
Email: suziep@electronicsworld.co.uk

GROUP SALES MANAGER:
Sunny Nehru
Tel: +44 (0)20 7062 2539

DESIGN:
Tania King

PUBLISHER:
Wayne Darroch

ISSN: 1365-4675
PRINTER: Buxton Press Ltd

SUBSCRIPTIONS:
Subscription rates:
United Kingdom –
1 year print and digital - £68
2 year print and digital - £109
3 year print and digital - £143
1 year digital - £30 + VAT
2 year digital - £50 + VAT
3 year digital - £70 + VAT
International –
1 year digital - £30.00
2 year digital - £50.00
3 year digital - £70.00
Tel/Fax +44 (0)1635 879361/868594
Email: electronicsworld@circdata.com
www.electronicsworld.co.uk/subscribe

SJP business media

2nd floor,
St Mary Abchurch House,
123 Cannon Street,
London,
EC4N 5AU

Follow us on Twitter @electrowo

Join us on LinkedIn

Contents

Regulars

Features

Cover supplied by Analog Devices

Find out more on p6-7

Shrinking electronics overtakes AI, 5G and the IoT as top design trend for 2019

By Tom Gregory, Product Manager, 6SigmaET

From artificial intelligence (AI) hardware to 5G standardisation, advancements in edge computing to the Internet of Things (IoT), 2018 was a year of bold technology promises. Looking back at 2018, we can begin to evaluate which technology trend was worth the wait, and which was just hype.

As we enter 2019, many designers are left uncertain how to proceed. With each new technology trend comes a host of new expectations and design challenges for device designers and engineers.

As thermal simulation software provider that's working closely with design engineers, software supplier 6SigmaET was keen to understand the extent of these trends. We recently conducted research, involving over 100 electronics professionals, designers and engineers, to assess their priorities and predictions for 2019. Conducted at the UK's Electronics Design Show, the survey asked participants to identify the top trends they believe will define electronic design in the year ahead.

Despite the hype surrounding new disruptive technologies such as artificial intelligence and the Internet of Things, the number one trend recognised as defining electronic design in 2019 was the continued shrinking of electronic components and devices. Of those surveyed, 33% believe that shrinking device sizes will have more of an impact on electronics design in 2019 than new technology developments such as 5G, AI or IoT.

This was followed by the incorporation of IoT technologies, then the need for AI capabilities and the demand for longer battery life for devices.

Other trends, such as adding 5G capabilities to devices and making them more computationally powerful didn't rank as highly, whereas "making them greener and more sustainable" ranked the lowest in the poll, with a mere 2% of electronics designers calling it their top priority for 2019.

It's important that engineers remember the day-to-day considerations, so that issues such as thermal management and design don't get lost among the hype

Added to this are thermal management issues, especially as devices become smaller and are pushed closer together, giving rise to thermal complications that demand accurate, responsive thermal simulation solutions. At the same time, new technologies such as AI and the IoT are also bringing their own unique challenges and a host of new hardware requirements.

In the case of AI, thermal complications come with the new variety of hardware to support machine learning; hardware such as Google's new Tensor Processor Unit 3.0 (TPUv3) with its colossal demand for processing power. From a thermal perspective, however, this dramatic increase in processing density represents a minefield of potential complications – starting with the increased heat generated throughout the device, which will need managing. Such thermal considerations will be at the heart of electronic design in 2019.

Despite this need to focus on potential thermal complications, 6SigmaET's research suggests that many designers still aren't taking these considerations seriously enough. One such study, which surveyed over 350 electronics engineers, found that 40% consider thermal management to be of low importance, while 13% of engineers don't test the thermal performance of their designs at all. 6SigmaET's previous research also shows that many of today's engineers fail to run simulations and do not identify thermal complications until after a design is complete.

If engineers are going to successfully develop the complex designs needed to capitalise on technology trends such as AI and edge computing, this approach must change.

Clearly, 2019 will see a fundamental shift in the electronics landscape, with new technologies and expectations providing both opportunities and challenges for the engineering community. While focusing on these significant challenges, however, it's important that engineers remember the day-to-day considerations, so that issues such as thermal management and design don't get lost among the hype. The rush to adopt new and innovative technologies should not allow us to compromise on the quality or reliability of those technologies further down the line. EW

French researchers develop new mass-spectrometry technology to study particles on the nanoscale

A team of researchers from from CEA-Leti, the CEA Biosciences and Biotechnology Institute of Grenoble (BIG) and the Institute for Integrative Biology of Gif-sur-Yvette has demonstrated a new mass-spectrometry technology based on nanomechanical resonators that measures the mass of particles previously beyond the reach of current commercial systems. The solution was then used to measure the mass of a whole bacteriophage virus capsid, which has not been achieved before.

Current mass measurement technologies can weigh from several tons down to the mass of hydrogen atom, roughly one atomic mass unit, or Dalton (Da). Between these extremes, a gap in mass of several orders of magnitude has been unfilled; so far, no commercial technology could measure the mass of nanoscale objects in the megadalton (MDa) to gigadalton (GDa) range. Yet, this range is of great interest, since it includes most viruses, diverse biomarkers for conditions such as cancers and degenerative diseases, and synthetic nanoparticles for nanomedicine.

Mass is a key parameter for studying, characterising and identifying particles on the nanoscale. The nanomechanical mass spectrometry system demonstrated by the French team is the first to analyse particles in the MDa-to-GDa range with efficiency and high precision, and without relying on ionisation.

Nanomechanical resonators "ring" at a specific tone or frequency, and a particle landing on the surface of a resonator will change the resonator's frequency. The mass of the particle can then be inferred from this frequency change.

Previous attempts to realise nanomechanical mass spectrometers mimicked conventional systems and used electromagnetic processes to transport ionised analytes to the resonator, resulting in prohibitive sample losses and analysis time, where a single analysis could take weeks.

The team avoided ionisation altogether: first, their system uses a surface acoustic wave device to nebulise nanoparticles in solution into a mist of small droplets, which are then aspirated into a vacuum system. Then, particles are transported and guided toward the nanomechanical detector using a flow of carrier gas that propels and focuses them into a very narrow beam. Since this beam is still much larger (~ mm^2) than a nanomechanical resonator (~ μm^2), the team uses not one but an array of 20 nanomechanical resonators to detect the mass of as many incoming particles as possible.

"In the mass range we are targeting, particles weigh the equivalent of 1 million to 1 billion hydrogen atoms. It is an intriguing range where some particles, just like objects of everyday life, are constituted of an unspecific number of atoms, while others are known to contain specific numbers of atoms of defined masses: like small molecules, they have a defined molecular mass," said Sebastien Hentz, director of research at CEA-Leti. "This is the case, for example, of the bacteriophage T5 virus capsid we have analysed. To our knowledge, this is the highest molecular mass ever determined by mass spectrometry."

Miniature solar panels embedded in clothing can charge cellphones and wearables

Nottingham Trent University has found a way to embed miniaturised solar cells into yarn that can be knitted and woven into textiles. The clothing made of this fabric will then generate electricity to charge a mobile phone or a wearable device.

Professor Tilak Dias with the fabric that can generate electricity to 10V

Measuring only 3mm x 1.5mm, the cells can't be felt by the wearer, making garments appear normal, despite their ability to generate electricity. The cells are encapsulated in resin which allows the textile to be washed and worn like any other form of clothing.

"The electrical power demand of smart e-textiles has always been their Achilles's heel. Now we can create clothing and fabric that generate power in a sustainable way, doing away with the need to plug items into wall sockets, and reducing the demand on the grid whilst cutting carbon emissions," said project lead Professor Tilak Dias (left), of the university's School of Art & Design.

The Advanced Textiles Research Group made a proof of concept 5cm x 5cm textile with 200 embedded cells. The fabric generates between 2.5V and 10V and 80mW of power, enough to charge a mobile phone and a Fitbit. The researchers claim that 2,000 of these cells could generate enough power to charge a smartphone.

"This technology could revolutionise the way we think about solar power, clothing and wearables," said researcher Achala Satharasinghe, who developed the prototype. "With miniaturised solar cells we can generate power in a range of new ways, by utilising things like clothing, fashion accessories, textiles and more. It will allow mobile devices to be charged in more convenient ways than ever before."

IoT systems need high integration and small form factor power conversion devices

Tony Armstrong,
Analog Devices, Inc.

At the medium-to-low end of the power spectrum, there are modest power conversion requirements, such as those commonly found in Internet of Things (IoT) equipment, that necessitate the use of power conversion ICs that deal with modest levels of current. These are usually in the range of hundreds of milliamps of current, but that amount can be higher if there are peak power demands that are needed by an onboard power amplifier for the transmission of data or video. Accordingly, the proliferation of wireless sensors supporting the numerous IoT devices has increased the demand for small, compact, and efficient power converters tailored to space and thermal constrained device form factors.

However, unlike many other applications, many industrial and medical products typically have much higher standards for reliability, form factor and robustness. As you would expect, much of the design burden falls on the power system and its associated support components. Industrial and even medical IoT products must operate properly and switch seamlessly between a couple of power sources such as the ac mains outlet and a battery backup. Furthermore, great lengths must be taken to protect against faults, while also maximising operating time when it is powered from batteries to ensure that normal system operation is reliable regardless of what power source is present. Accordingly, the internal power conversion architecture used within these systems need to be robust, compact and require minimal heat sinking.

Power Supply Design Considerations

It is not unusual for an industrial IoT system designer to use linear regulators in a system that incorporates wireless transmission capability. The primary reason being that it minimises EMI and noise emissions. Nevertheless, although switching regulators generate more noise than linear regulators, their efficiency is far superior. Noise and EMI levels have proven to be manageable in many sensitive applications if the switcher behaves predictably. If a switching regulator switches at a constant frequency in normal mode, and the switching edges are clean and predictable with no overshoot or high frequency ringing, then EMI is minimised. Moreover, a small package size and high operating frequency can provide a small, tight layout, which minimises EMI radiation. Furthermore, if the regulator can be used with low ESR ceramic capacitors, both input and output voltage ripple, which are additional sources of noise in the system, can be minimised.

It is common for the main input power to today's industrial and medical IoT devices to be a 24V or 12V dc source from an external ac-to-dc adapter and/or battery bank. This voltage is then further reduced to either 5V and/or 3.xV rails using synchronous buck converters. Nevertheless, the number of internal postregulated power rails in these medical IoT devices has increased, while operating voltages have continued to decrease. Thus, many of these systems still require 3.xV, 2.xV or 1.xV rails for powering low power sensors, memory, microcontroller cores, input/output and logic circuitry. Nevertheless, the internal power amplifier used for data transmission can require a 12V rail with up to 0.8A of current capability to transmit any recorded data to a remote centralised hub.

Traditionally, this 12V rail has been supplied by step-up switching regulators and required specialised switch-mode power supply design know-how, as well as a large solution footprint on the printed circuit board (PCB).

A New Compact Boost Converter

Analog Devices's µModule (micromodule) products are complete system-in-package (SiP) solutions that minimise design time and solve the common problems of board space and density issues commonly found in industrial and medical systems. These µModule products are complete power management solutions with integrated dc-to-dc controllers, power transistors, input and output capacitors, compensation components and inductor within a compact, surface-mount BGA or LGA package. Designing with ADI's µModule products can reduce the amount of time needed to complete the design process by up to 50%, depending on the complexity of the design. The µModule family transfers the design burden of component selection, optimisation and layout from designer to the device, which shortens the overall design time and system troubleshooting, as well as ultimately improving time to market.

Furthermore, ADI's µModule solutions integrate key components commonly used in discrete power, signal chain and isolated designs

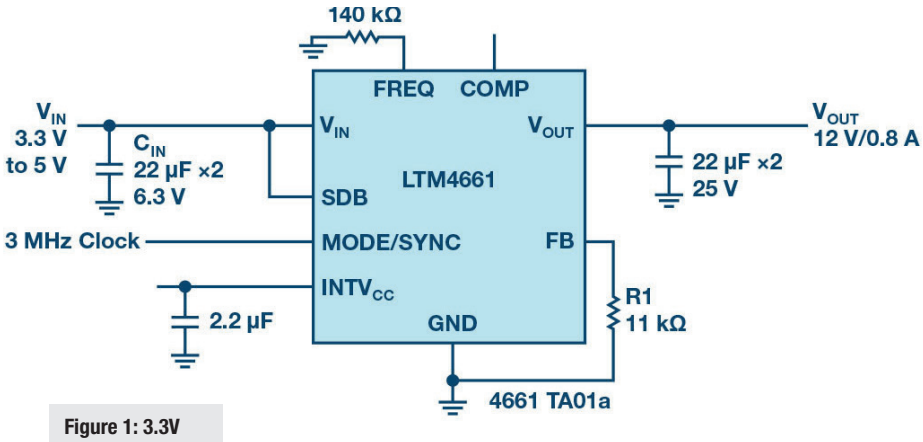

Figure 1: 3.3V to 5V input, delivering 12V at up to 800mA with an external clock

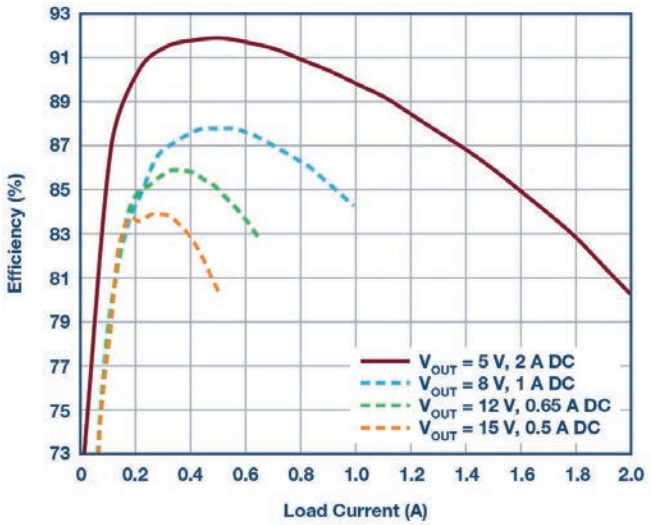

Figure 2: Efficiency vs. output current for the LTM4661 from a 3.3V input to outputs ranging from 5V to 15V

within a compact, IC-like form factor. Supported by ADI's rigorous testing and high reliability processes, the µModule product portfolio simplifies the design and layout of power conversion designs.

The µModule family of products embraces a wide range of applications including point of load regulators, battery chargers, LED drivers, power system management (PMBus digitally managed power supplies), isolated converters, battery chargers and LED drivers. As highly integrated solutions with PCB Gerber files available for every device, µModule power products address time and space constraints while delivering a high efficiency, reliable and, with select products, low EMI solution compliant with EN 55022 Class B standards.

As design resources become stretched by increased system complexity and shortened design cycles, the focus falls on development of the key intellectual property of the system. This often means neglecting the power supply until late in the development cycle. With little time and perhaps limited specialist power design resources, there is pressure to come up with a high-efficiency solution with the smallest possible footprint, while potentially utilising the underside of the PCB as well for maximum space utilisation.

This is where the µModule regulator provides an ideal answer. The concept is complex on the inside, simple on the outside - the efficiency of a switching regulator and the design simplicity of a linear regulator. Careful design, PCB layout, and component selection are very important in the design of a switching regulator and many experienced designers have smelt the distinctive aroma of burning circuit board in the earlier days of their career. When time is short or power supply design experience is limited, the ready-made µModule regulator saves time and reduces risk.

One recent example from the ADI µModule family is the LTM4661 synchronous step-up µModule regulator, which is available in a 6.25mm × 6.25mm × 2.42mm BGA package. Included in the package are the switching controller, power FETs, inductor and all support components. Operating over an input range of 1.8V to 5.5V, it can regulate and output voltage of 2.5V to 15V, and is set with a single external resistor. Only a bulk input and output capacitor are needed.

Figure 3: Thermal image of LTM4661, 3.3V input to 12V output at 0.8A, 200 LFM air flow, and no heat sink

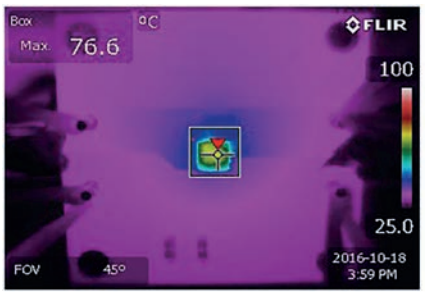

The LTM4661 is efficient and can deliver efficiencies of greater than 87% when stepping up from a 3.3V input to a 12V output. See the efficiency curve in Figure 2.

Figure 3 shows the measured thermal picture of the LTM4661 running from a 3.3V input to 12V at 800mA dc current with 200 LFM airflow and no heat sink.

Conclusion

The deployment of IoT equipment has exploded in recent years and includes a wide variety of products for the military and industrial application spaces. A new wave of products, including sensor-filled medical and scientific instrumentation, has been a key market driver in recent years and is now starting to see signs of significant growth. At the same time, the space and thermal design constraints of these systems has necessitated a new class of power converters that can deliver the necessary performance metrics of small, compact and thermally efficient footprints to power the internal circuits, such as the power amplifier. Fortunately, devices such as the recently released LTM4661 step-up µModule regulator elevates the power supply designer's task.

Finally, using µModule regulators make sense in these types of applications since they can significantly reduce debug time and allow for greater board area usage. This reduces infrastructure costs, as well as the total cost of ownership over the life of the product.

Analog Devices (UK) Ltd
Tel: 01628 477066
Email: uksales@linear.com
www.analog.com

Artificial intelligence will change cobots from collaborators into true partners

By Mark Patrick, Mouser Electronics

It'll be a true game-changer when cobots can be taught what to do without complex programming. It'll be even more exciting when they can learn independently, based on their experiences. For that we turn to artificial intelligence (AI), and there are already examples today of some advanced cobots showing what's possible through learning and autonomy.

Human-Like Learning Qualities

We've always collectively imagined robots to have a human-like brain, making their own decisions. Cobots will make this happen; they could optimise what they're doing in real time, based on what their sensors are telling them. If they encountered a situation where they didn't know what to do, they could ask a human, and listen to verbal instructions, instead of programming. AI can help achieve this kind of autonomy and more in cobots.

Of course, there are some highly autonomous robots out there already, but they typically cost tens to hundreds of millions of dollars. For similarly capable cobots to become a viable option for industry, the cost needs to be a fraction of these prices, and this is where the growing cobotics industry and academia are working hard.

AI: Start Small and Expand

AI is a broad area, but for cobotics the first focus is machine learning, whereby a cobot gradually learns from its experiences to improve its abilities. This branch of AI uses algorithms that enable the cobot to make predictions, which in turn enables it to make its own choices.

Perception is another must-have: the machine needs to use data from its sensors to produce a 'vision' of its surroundings, to which it can then respond. This is essential to ensure that cobots can operate safely alongside humans.

Cobots' basic motions and object-handling don't necessarily require AI, but if the robot needs to be able to navigate autonomously, localise, map or plan a journey, sensor-enabled AI becomes essential.

Another area where AI plays a major role is natural language processing, which will mean cobots can converse with and learn from human operators. Basic verbalisation in cobots is already a reality, but there's more to be done, drawing on several strands of AI.

Cobots' basic motions and object-handling don't necessarily require AI, but if the robot is to navigate autonomously, localise, map or plan a journey, sensor-enabled AI becomes essential

Artificial neural networks will play an important role in the future as well. These aim to enable sophisticated learning without having to program the robot – much like the way the human brain operates. Artificial neural networks are extremely complex, their main goal being to enable robots' motors to respond appropriately to different inputs from their sensors, even when their surroundings change.

Lastly, there's deep learning, the most sophisticated form of machine learning, which effectively is a multi-layered ('deep') neural network, also inspired by the human brain. Deep learning uses a series of trainable components to recognise objects, with each stage being used for training. It offers the potential to develop and use algorithms directly, although the amount of processing power and data it requires make it a future aspiration in cobotics, rather than something achievable in the short term.

State-Of-The-Art Cobotics Examples

Carnegie Mellon University's Robotics Institute has developed autonomous mobile service robots that can move around the centre's office buildings, navigating hallways, lifts and open spaces to deliver goods. They can transfer loads between themselves and communicate to optimise their delivery routes for maximum efficiency. This includes notifying one another if routes are blocked (so others can dynamically re-route to avoid them) or if a door to an office is closed (so another cobot due to make a delivery there knows to postpone the drop-off until the office occupant is back). They can even ask humans for help.

Areas where people are continually moving around or where furniture often gets shifted – such as a restaurant or hospital, for example – are handled using an algorithm based on Episodic non-Markov Localisation (EnML). This enables the cobot to make assumptions about items, without having to store large volumes of data, as static mapping would require. Moreover, the cobot needn't store a full history of everything it's ever observed or done.

Elsewhere, the German Fraunhofer Institute for Computer Graphics Research has produced a cobot capable of independently scanning parts and then printing them in 3D in real time. The robot moves its scanning arm around the component, using algorithms to produce a 3D image. It then verifies the accuracy of the scan and prints the part. None of this requires programming, manual training or computer-aided design tooling.

Exciting Future for Cobots

These examples highlight what's already possible, and as AI develops further, exciting and potentially revolutionary cobotic capabilities will follow, most likely one step at a time. The result will be cobots that aren't simply collaborators but true partners. EW

A low-power, low-cost, differential input to a single-ended-output amplifier

By Chau Tran and Jordyn Rombola, Product Engineers, Analog Devices

Question:

How to make a low-cost, low-power, differential input into a single-ended-output amplifier?

Answer:

In many applications there are requirements for low-power, high-performance differential amplifiers to convert small differential signals to readable ground-referenced output signals.

Input voltages at two inputs usually share a large common-mode voltage. The differential amplifier rejects the common-mode voltage, and the remaining voltage is amplified and presented on the amplifier output as single-ended. The rejected voltage can be either AC or DC, and this common-mode voltage is typically larger than the differential input voltage.

The effectiveness of the rejection diminishes as the frequency of the common-mode voltage increases. Amplifiers within the same package have better matching, the same parasitic capacitance and need no external wiring. Therefore, a high-performance, high-bandwidth dual amplifier performs better with frequency than two discrete amplifiers.

Simple Solution

A simple solution is to use dual precision amplifiers with a resistive gain network, as shown in Figure 1. This circuit shows a simple way of converting a differential input to a single-ended output with adjustable gain. The gain of the system can be set by the following equation:

$$V_{OUT} = -Gain \times (V_{IN}1 - V_{IN}2)$$

where gain = RF/1kΩ and ($V_{IN}1 - V_{IN}2$) is the differential input voltage.

Generally, this technique provides a more stable reading when EMI or RFI is present and therefore is recommended when noise is a problem. This is especially true when measuring thermocouple, strain gage or bridge-type pressure sensor inputs, since they produce very small signals in a noisy environment.

This circuit can offer a performance improvement over single-ended inputs by not only measuring the difference in voltage between the positive and negative terminals of the sensor, but also providing common-mode rejection with some system gain. Furthermore, the sensor ground can be different from the analogue ground. An output voltage referenced to

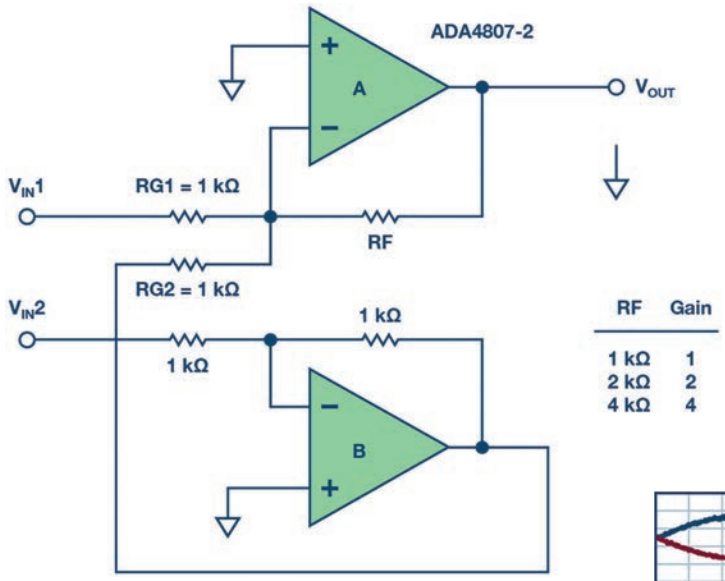

RF	Gain
1 kΩ	1
2 kΩ	2
4 kΩ	4

Figure 1: Differential input, single-ended output amplifier

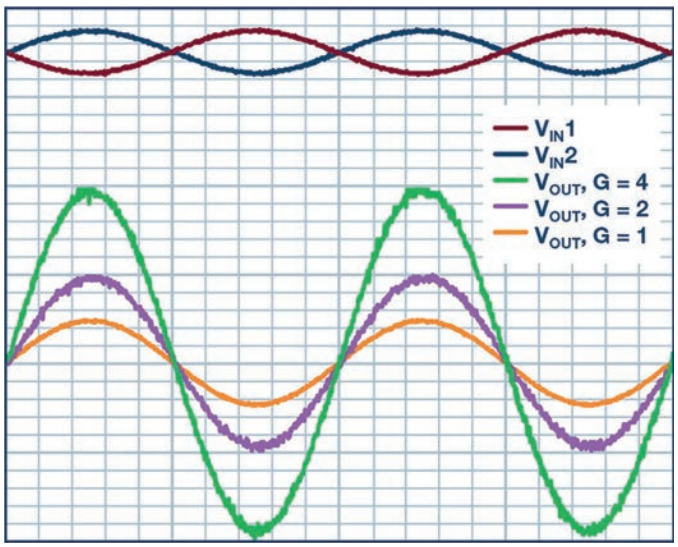

Figure 2: The performance of a simple differential to single ended amplifier

ground is important in many applications; the accuracy of the system depends on the tolerance of the network resistors.

The circuit can convert a differential input to a single-ended output with adjustable gain. The gain of the system is set by the ratio of RF and RG1 with the assumptions that RG2 = RG1 and amplifier B has a gain of –1.

Example Amplifier

The ADA4807-2 is a 180MHz dual amplifier that can be realised as an inverting amplifier for this application, providing lower noise. With a low quiescent current of 1000µA per amplifier, the circuit is ideal for low-power, high-resolution data-conversion systems.

The input common mode can go beyond supply voltages. The output is rail-to-rail, which makes it useful in the presence of a large common-mode signal or large output voltage application. For example, the data acquisition board has an ADC that accepts a single-ended input of 0-5V. However, the signal source happens to be differential voltage, generated from a sensor bridge where one terminal swings positive while the other goes negative in response to the presence of common noise.

The plot in Figure 2 was taken by applying a differential input voltage and varying the circuit's gain. The RF value sets the gain of the system. The plot shows the system gain of 1, 2 and 4, with the differential input voltage of $1V_{p-p}$ at 1kHz.

The circuit is useful for measuring a small difference between two large voltages. For example, consider a solution with a simple 1% accuracy of monitoring a typical Wheatstone bridge circuit excited by 3V/GND in a 3V battery-powered system. Using 1% resistors or better will allow for high accuracy, and the circuit will reject any common mode and amplify the attenuated bridge signal by the gain it is set for. If driving an ADC, some level-shifting will need to be applied to get the output signal in the range of 0-5V.

This circuit offers a combination of excellent distortion with low quiescent current. The two-opamp solution results in lower system cost and better performance when using a differential amplifier. EW

Analogue Input Modules for a -5V to +5V to 0-5V Signal Converter

By Dr. Murat Uzam, Academic and Technical Author, Turkey

This column describes a project involving thirteen analogue input modules and seven analogue output modules for a 5V microcontroller through its ADC and DAC channels.

In previous columns, we discussed the analogue input modules for a 0-5V signal converter, which accept DC input voltages from 0V to 6.26V, 12V and 24V, and require different DC power supplies.

In the most recent column, we analysed the analogue input modules for a 0-10V to 0-5V signal converter, which accept DC input voltages from 0V to 24V and require 6.26V, 12V and 12V DC power supplies, respectively. This month, we will focus on the analogue input modules of a 2-5V to 5V to 0-5V signal converter.

The -5V to ±5V to 0-5V signal converter input module 1 (and then respectively 2) can accept DC input voltages from -12V to 12V, and requires four DC power supplies, 5V, 6.26V, -12V and 12V, or only two DC power supplies, -12V and 12V.

Analogue Input Module 1

Figure 1 shows the diagram of module 1 of the -5V to 5V to 0-5V signal converter, with Figure 2 showing its connections to an analogue input of a 5V microcontroller. In this design we assumed that the input voltage range V_{IN} is -12V to 12V. When -12V < V_{IN} < -5V, V_{OUT} = 0V. When -5V ≤ V_{IN} ≤ 5V, V_{OUT} = (V_{IN} + 5V)/2. When +5.01V ≤ V_{IN} ≤ 12V, V_{OUT} will be equal to a value from 5.01V to 5.07V, due to the electrical properties of the LM358P-2A used.

Figure 1: Schematic of analogue input module 1 of the -5V to 5V to 0-5V signal converter, to be used with an ADC input of a 5V microcontroller

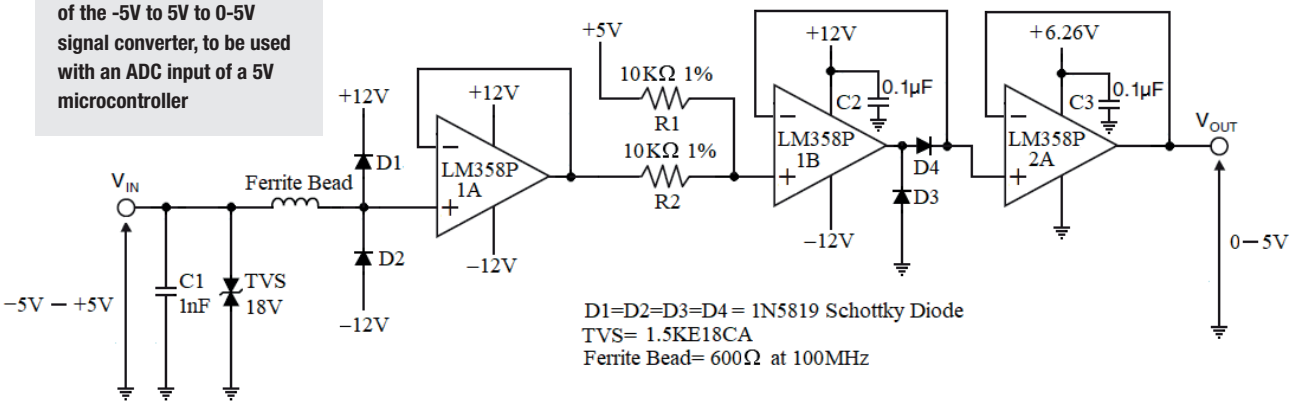

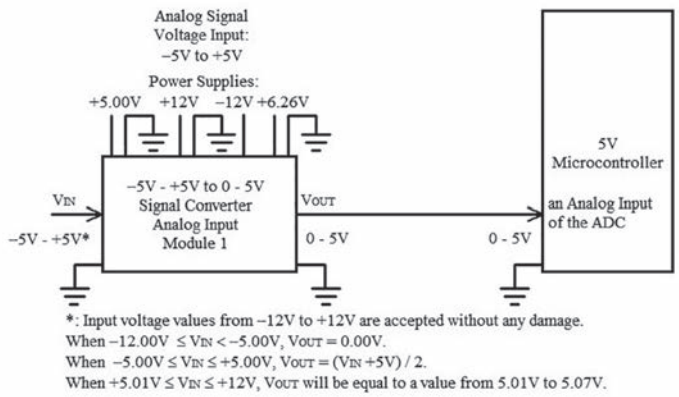

Figure 2: Connecting the signal converter

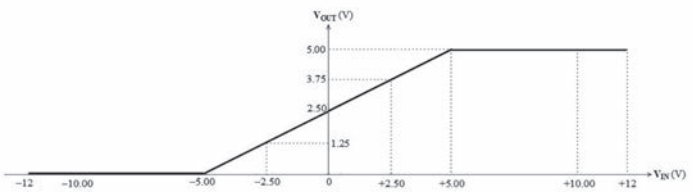

Figure 3: V_{OUT} vs V_{IN} for the signal converter

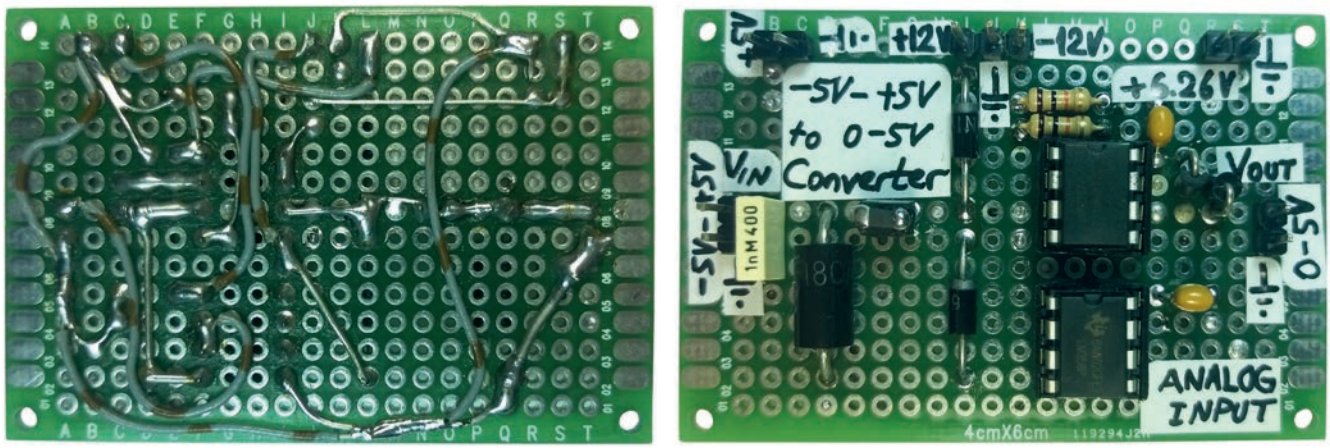

Figure 4: Top and bottom of the prototype breadboard of analogue input module 1 of the -5V to 5V to 0-5V signal converter

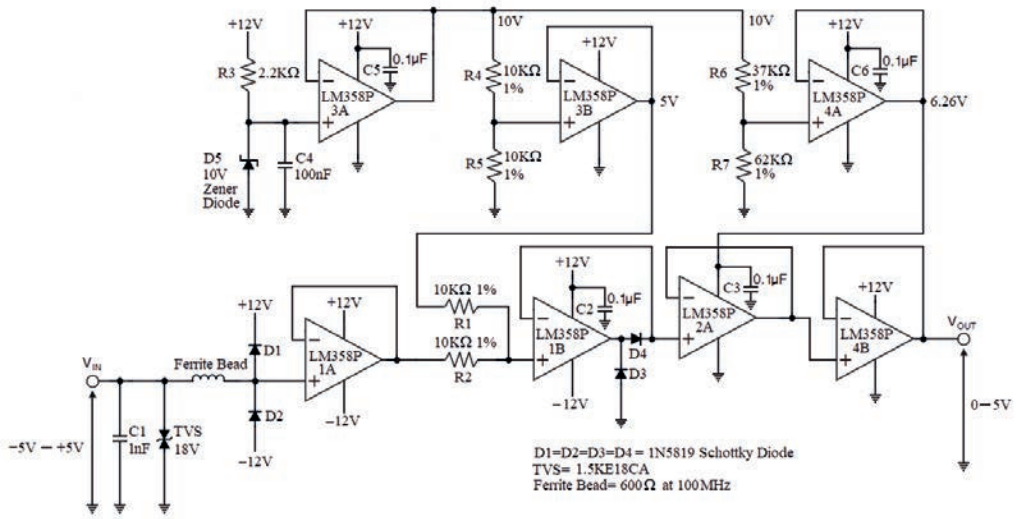

Figure 5. Schematic diagram of the signal converter – analogue input module 2

The relationship between V_{OUT} and V_{IN} is shown in Figure 3. It can be seen that input voltages to +12V are accepted without any damage to the circuit, and are output as a value from 5.01V to 5.07V.

This design is used to level-shift the bipolar -5V to 5V analogue voltage signal to provide a unipolar 0-5V analogue input signal.

When $-5V \le V_{IN} \le 5V$, this circuit acts as a non-inverting summing amplifier with the transfer function:

$$V_{OUT} = \left(\frac{R1}{R1 + R2}\right) V_{IN} + \left(\frac{R2}{R1 + R2}\right) 5$$

Since R1 = R2:

$$V_{OUT} = \left(\frac{1}{2}\right) V_{IN} + \left(\frac{1}{2}\right) 5 = \frac{V_{IN} + 5}{2}$$

It performs analogue summation between V_{IN} and 5V with gain of 1. Analogue inputs are subject to electric surge or electrostatic discharge on their external terminal connections. The TVS (transient voltage suppressor) shown in the circuit provides highly effective protection against such discharges. A ferrite bead is connected in series with the input path to add isolation and decoupling from high-frequency transient noise.

External Schottky diodes generally protect the operational amplifier. Even when internal ESD protection diodes are provided, the use of external diodes lower noise and offset errors. Dual series Schottky barrier diodes D1 and D2 divert any overcurrent to the positive or negative power supply. The operational amplifier LM358P-1A, with bipolar supply voltages, provides a high input impedance and is connected as a buffer amplifier (voltage follower). +5V and R1, V_{IN} and R2, and LM358P-1B act as a non-inverting summing amplifier. Diodes D3 and D4 ensure that when $-12V \le V_{IN} < -5V$, $V_{OUT} = 0V$. The operational amplifier LM358P-2A, with a 6.26V supply, acts as a voltage limiter and is connected as a buffer amplifier (voltage follower). V_{OUT} is obtained from the output of the LM358P-2A.

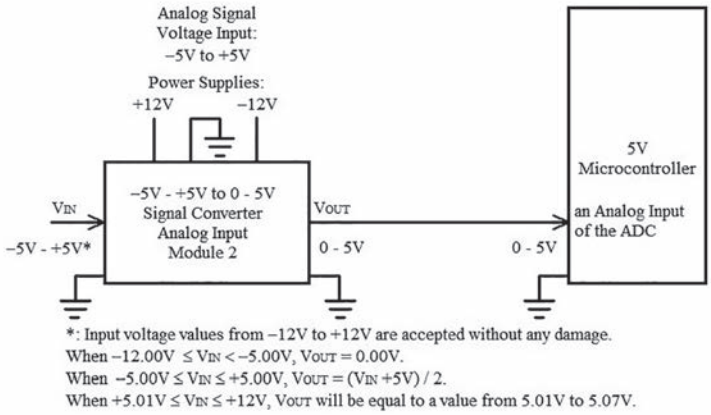

Figure 6: Connection of the -5V to 5V to 0-5V signal converter – analogue input module 2

Table 1 shows some example input and output voltage values for analogue input module 1 of the -5V to +5V to 0-5V signal converter. Top and bottom of its prototype breadboard are shown in Figure 4.

One important implementation tip for proper operation is to ensure that R1 = R2 and +5V = +5V.

V_{IN}(V)	V_{OUT}(V)
+12.00	5.0X
..	5.0X
+10.00	5.0X
..	5.0X
+5.00	5.00
..	..
+4.00	4.50
..	..
+3.00	4.00
..	..
+2.50	3.75
..	..
+2.00	3.50
..	..
+1.00	3.00
..	..
0.00	2.50
..	..
-1.00	2.00
..	..
-2.00	1.50
..	..
-2.50	1.25
..	..
-3.00	1.00
..	..
-4.00	0.50
..	..
-5.00	0.00
..	..
-10.00	0.00
..	..
-12.00	0.00

Table 1: Some example input and output voltage values for analogue input module 1 of the -5V to 5V to 0-5V signal converter

5x is a value from 5.01V to 5.07V

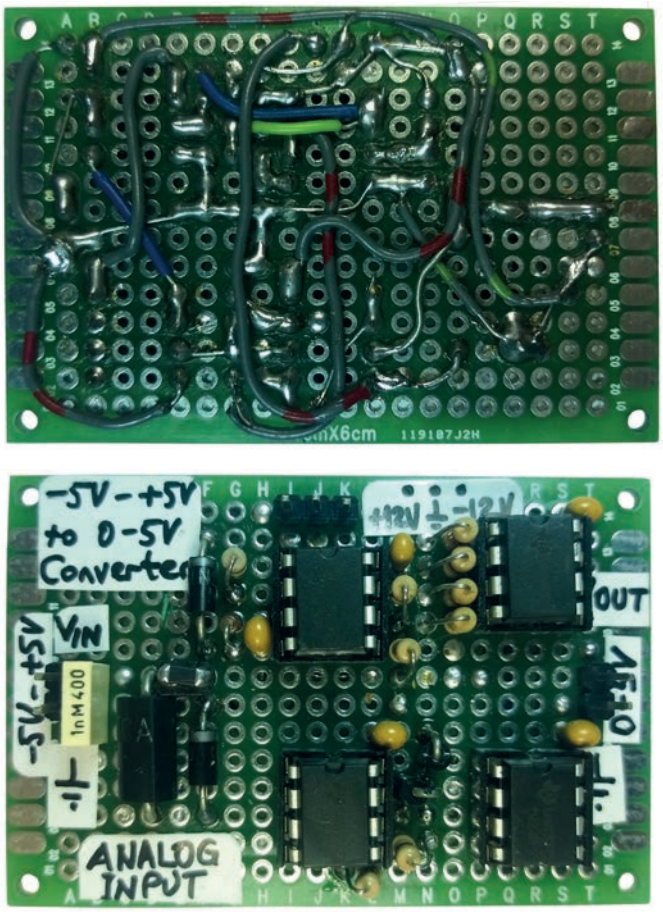

Figure 7: Top and bottom of the prototype circuit board of -5V to 5V to 0-5V signal converter's analogue input module 2

Figure 5 shows the schematic diagram of the analogue input module 2 of the -5V to 5V to 0-5V signal converter, used with the ADC input of a 5V microcontroller. Its connections are shown in Figure 6.

As with the previous module, in this design we assumed that the input voltage range V_{IN} is -12V to 12V. When -12V ≤ V_{IN} < -5, V_{OUT} = 0V. When -5V ≤ V_{IN} ≤ +5V, V_{OUT} = (V_{IN} + 5V)/2. When 5.01V ≤ V_{IN} ≤ 12V, V_{OUT} will be a value from 5.01V to 5.07V, due to the electrical characteristics of the LM358P-2A used. Again, the relationship between V_{OUT} and V_{IN} is shown in Figure 3.

Except for the buffer amplifier LM358P-4B from which the output voltage V_{OUT} is obtained, the lower part the diagram in Figure 5 is identical with that of the analogue module 1 of the -5V to +5V to 0-5V signal converter shown in Figure 1. The upper part obtains both the 5V and 6.26V reference voltages. R3, D5 (10V zener diode) and C4, together with buffer amplifier LM358P-3A, provide a 10V reference voltage from a 12V power supply. This is then divided by resistors R4 and R5 to obtain a 5V reference voltage.

Next, the 5V reference voltage is connected to the non-inverting input of the buffer amplifier LM358P-3B, whose output is fixed as a 5V reference voltage capable of sourcing up to 20mA.

Likewise, the 10V reference voltage is also divided by R6 and R7 to obtain a 6.26V reference voltage. This 6.26V reference voltage is connected to the non-inverting input of buffer amplifier LM358P-4A, whose output is fixed as a 6.26V reference voltage sourcing up to 20mA.

Table 1 provides some example input and output voltages. The top and bottom of this module's prototype breadboard are shown in Figure 7. For proper operation make sure that R1 = R2, R4 = R5 and R7/(R6 + R7) = 62.62%. EW

NEW

PSY280 Series AC-DC power supplies can provide up to 300W of output power in a compact 2” x 4” footprint!

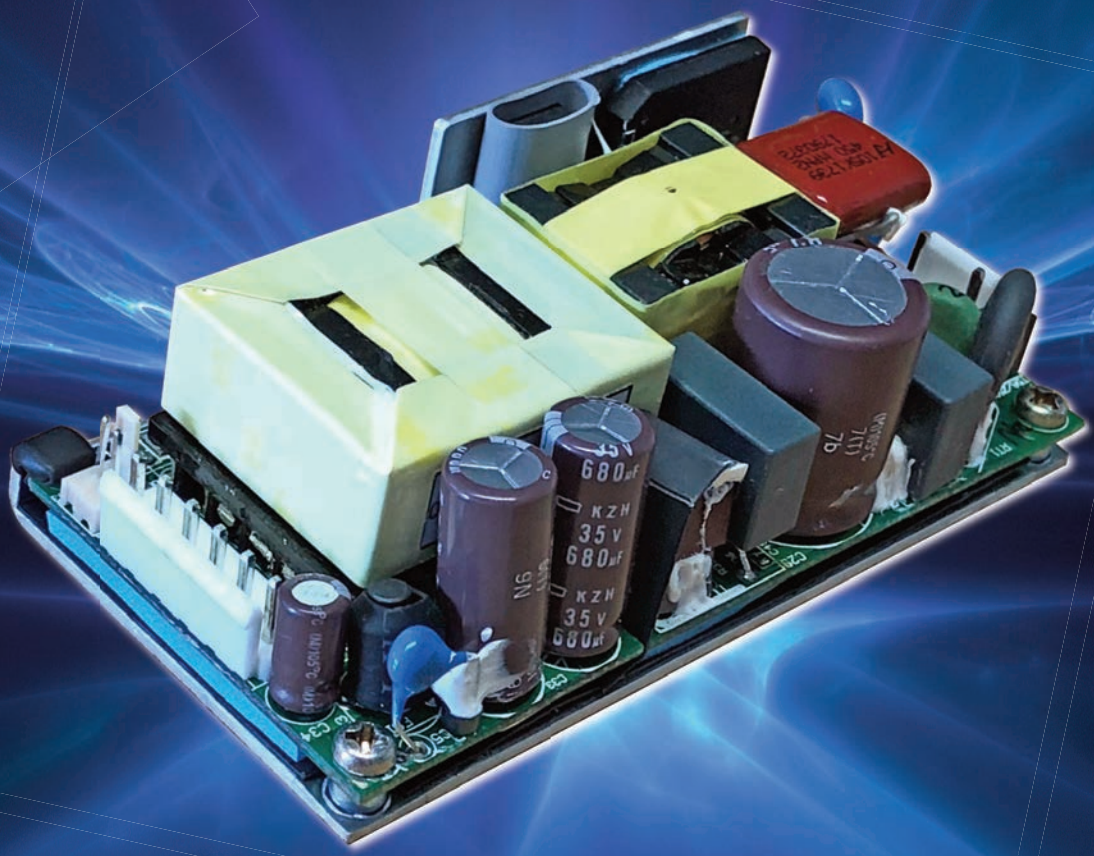

The new Powersolve PSY280 Series compact AC-DC converters can give up to 300 Watts of output power. This compact unit with universal AC input has 6 standard single output models with voltages ranging from 12V to 54VDC. It can deliver 150W convection cooled, 180W conduction cooled via its aluminium chassis, 280W forced air cooled and 300W with conduction and forced air cooling. Operating temperature is -30°C up to +85°C.
No load power consumption is less than 0.15 Watt.

POWER SOLVE

www.powersolve.co.uk

Tel: 01635-521858 Email: sales@powersolve.co.uk

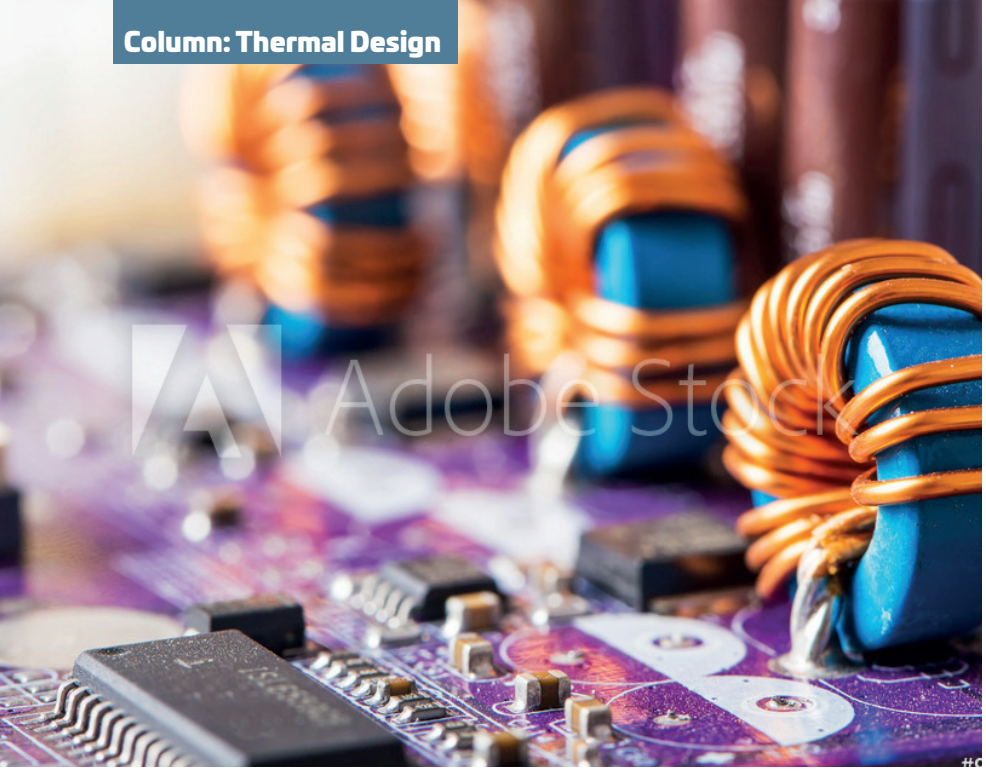

The reasons electronics engineers must commit to thermal neutrality

Chris Aldham,
Product Manager,
6SigmaET

In 2019, other industry suppliers are expected to come on board and support the adoption of a truly neutral file format

For today's electronics engineers, balancing power, heat and performance in their designs has become much more difficult. As devices become smaller yet more complex, thermal performance becomes ever more important. At the same time, as engineers have looked to reduce the costs and timelines involved in their designs, the feasibility of physically testing devices has decreased. Instead, a growing number of engineers now rely on simulation to test the thermal implications of their designs – 6SigmaET's research suggests over 40%.

But, it's not just device designers who need to consider potential thermal complications. As components inside devices become increasingly complex, the use of thermal simulation has infiltrated the entire supply chain – from the most basic internal components right through to the end product.

Simulation in the Supply Chain

As the number of interwoven manufacturers, designers and engineers using simulation software increases, so too does the complexity of using a non-standardised file format.

Unlike in CAD, with its many cross-platform "neutral" file formats (such as SAT, STEP, IGES, IDF or GERBER), each thermal simulation software platform uses its own proprietary format. Traditionally, these formats can't be used outside the software they were created in, and they often can't be exported to other simulation suites. As a result, it's almost impossible to exchange thermal simulation data between teams, customers and suppliers, or to use different simulation tools.

For the most part this has not been a major issue for design engineers as, once a designer has committed to a particular thermal simulation platform, they are unlikely to deviate from it for years to come. In fact, according to our research, 40% of thermal engineers have never switched simulation tools, while a further 18% haven't switched for over three years. Not only has this commitment reduced the need for a neutral file format, it has also proved lucrative for thermal simulation software suppliers who know their customers will stay for life.

Another issue is that thermal simulations are now passed along the component supply chain, adding a new layer of complexity. Thermal models are being developed in different platforms, for different components, all the way down the supply chain. If created using different software, the resulting file formats are of no use to the end product designer. As a result, component suppliers are forced to either use their customers' preferred thermal modelling platforms, or to completely rebuild their models from scratch every time they want to export a design.

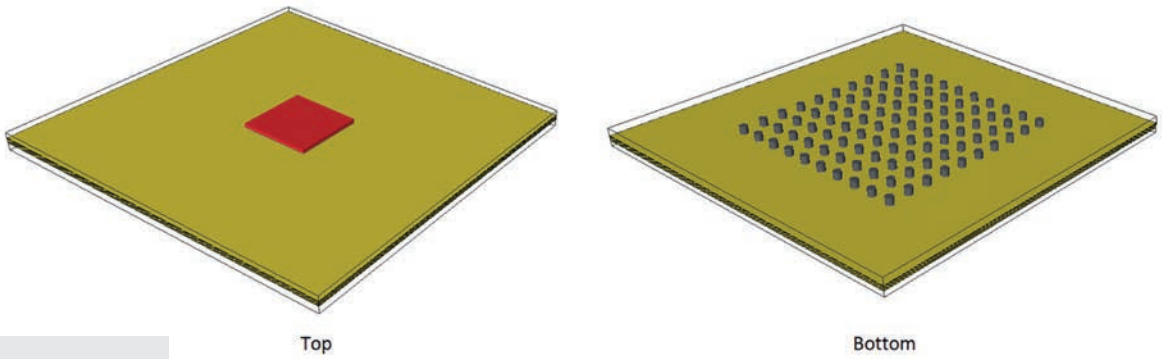

Flip chip example

For large component suppliers such as Intel, this means providing multiple models of each component, to make sure that any designer can integrate them without complication. This process often represents hundreds of lost man-hours rebuilding designs, at a significant cost to both supplier and end-device designer.

The Need for a Neutral File Format

Given this dramatic change in the thermal simulation landscape, it's become clear that using multiple propriety file formats for thermal simulation is not good enough. Instead, what's needed is a single, cross-platform neutral file format for computation fluid dynamics (CFD) models of electronics.

To address this need, Future Facilities – makers of the 6SigmaET thermal simulation software – joined with Intel and other simulation software suppliers to address the issue. Joining a public forum at Semi-Therm in March 2018, the group outlined its vision for a potential future neutral file format for thermal simulation. The aim was to produce a human-readable XML-based format that's simple to implement for each vendor.

Making Neutrality a Reality

Having listened to this feedback, Intel – working with Motorola Mobility – put forward its proposal for a vendor-neutral file format, with David Ochoa, data centre platform applications engineer at Intel, concluding: "After visiting multiple customers, it's clear that the thermal engineering community must establish a neutral model file format. Intel would like to propose the adoption of a neutral file format to help engineers exchange thermal model data from components to system-level, regardless of the software package used."

After Intel and Motorola Mobility announced their required specifications for a neutral file format, thermal simulation vendors were quick to develop and incorporate their own cross-platform file types that meet the strict requirements.

In 2018, following the Semi-Therm discussion, an XML-based ECXML neutral file format was launched. Shortly thereafter, Cadence announced that its Sigrity PowerDC Technology will also adopt the neutral file format. And, in December, Ansys announced its support of the Neutral File Format. 6SigmaET has already incorporated it into its solutions.

In 2019, other industry suppliers are expected to come on board and support the adoption of a truly-neutral file format. Once this file type and structure has gained wider acceptance, plans are to officially standardise it via a traditional industry body such as JEDEC. This is not only good news for suppliers, who will no longer have to develop multiple models for their designs, but also for all simulation software users who will have a freer choice of platforms and the opportunity to switch between suppliers to get the fastest and most accurate simulation results for their designs. EW

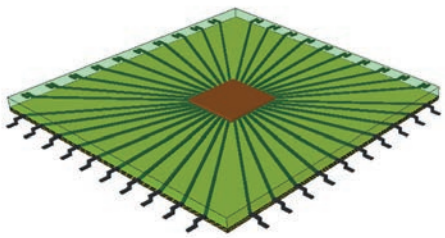

Example component model

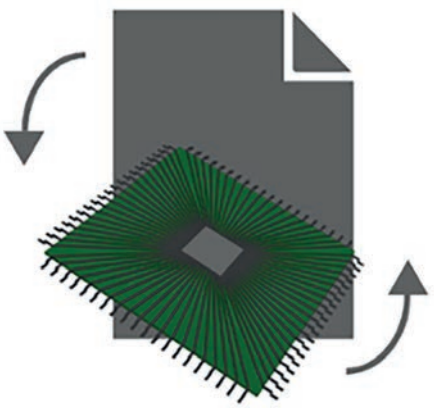

NFF file exchange

Q&A with...

Duane Benson

chief technology officer (CTO) at Screaming Circuits, a division of Milwaukee Electronics

... who discusses his technology predictions for 2019 – and beyond

Q **What will be the main technology trends in 2019?**

A We're coming into 2019 for a wild ride. The last few years have been pretty crazy, and 2019 looks to continue that trend. These are the things I predict we will work on in the next decade:

1: Artificial intelligence (AI) will go mainstream;
2: Safer highways;
3: Radically-changed healthcare;
4: IoT (Internet of Things) finally works;
5: We get security figured out.

Q **Artificial intelligence is currently a buzzword in the industry; some see it as a positive force, others as a potentially negative one. Which way do you believe it's likely to go?**

A I see a slightly different perspective than I've seen from most others. I don't see "the machine" taking over the world and us, but one that can help our human purposes run smoother and more efficiently.

AI will become mainstream in the next decade. The machine won't be sentient but will largely be indistinguishable from humans. We just need to work hard to ensure that it can appropriately deal with the negative human elements or we'll be surrounded by depressed, disrespectful and angry machines.

Q **Fully automated vehicles are another technology in which many companies are currently investing. What shall we look forward to in this field?**

A I believe by the end of the decade, virtually all commercial vehicles up to 20% of personal vehicles will be connected. Autonet is a segment of the Internet dedicated to moving vehicles. It's designed to allow for collective awareness of everything that may be of concern to a vehicle. Instead of just being aware of its immediate surroundings, with Autonet all sensors data and processing capability of networked vehicles are integrated into an awareness dataset and made available to anything on the net.

With Autonet connection, all vehicles within their specific lanes will effectively act as one. They will be capable of faster speeds while staying much closer together – and still being far safer than they are today. Rather than continually widening motorways, this automotive "automation" will eventually increase existing motorway capacity by a significant amount.

Q

How do you see healthcare improving?

A

We are on the verge of a complete shift in the way technology and health interact. It will be as big a change to daily life as what happened with the introduction of the personal computer, Internet and smartphone.

Today, wellness is a thing. It largely consists of encouraging regular checkups, improving diet and increasing activity, all with the aim of reducing costs for insurance carriers. This is a good thing but not good enough, because part of the problem with today's wellness trend is that it's built on the healthcare technology advances of the past three decades.

In five to ten years, we may see the first usable organs for transplant grown out of our own cells. A scaffold will be 3D-printed with a dissolvable structure. Skin cells from the recipient will be converted into T-cells programmed to grow around the scaffold and become a kidney, liver or other organ. That organ will then be implanted without the need for anti-rejection drugs.

Along with 3D printing, subcellular engineering will come into being. Designer viruses will become a viable means of curing many cancers and other serious afflictions. Virus programming will eventually allow for fast and effective treatment of almost all known ailments.

Q

Wouldn't this approach increase costs needed to support it?

A

The first such treatments will cost millions of dollars, maybe tens of millions. But when the T-cells are injected and programmed to rebuild the organ in situ, costs and level of infrastructure needed drop to a small fraction of their peak. When the human body is largely rebuildable via injection (probably 20-30 years down the road), healthcare becomes no more serious than auto repair.

Q

What about IoT – our industry has talked a lot about it; do you believe it has met our expectations?

A

Interoperability is still questionable at best. Within the next decade, standards, protocols and security technology will reach the point where adding to your IoT life will be no more difficult than plugging in a toaster.

Going that last mile to make things easier is often more difficult than all the time spent earlier, but it's the most important. We won't be able to fully take advantage of all the Internet has to offer until it is that easy. I'm seeing that in another five to ten years.

Q

In each of these fields we touched on today, security is seen of great importance. How will this be addressed in the near future?

A

Security, like ease of use, is prerequisite to fully engaging the potential of a connected world. Today, with all the distance we've come, social engineering – a human contacting a human – is still the biggest class of security vulnerability. We will always need improvements in technology security, but it will never be enough without solving the human problem.

I wish I knew what the solution will be. That would be a great business to go into, but it's way beyond me. Someone will figure this out within the next decade and when they do, a lot of unrealised potential will suddenly open up. In fact, my four predictions above all depend on this happening.

Improved phase-locked loop method for grid synchronisation of wind energy systems

By Fehmi Sevilmiş and Hulusi Karaca, Selçuk University, Turkey

Fossil-based energy sources have significantly influenced human life, but not always positively, considering their impact on the climate. Now we are now seeing a rise in environmentally-friendly renewable energy sources, one of which is wind energy, a clean, economic, sustainable and reliable type. Countries like China, the US, Germany and Denmark are all increasing their production of electricity from wind energy.

The annual and cumulative installed global wind-power values for 2002-2017 are shown in Figures 1 and 2, respectively. In 2017, the installed global wind power capacity was close to 52.5GW. The cumulative global installed wind power by the end of 2017 reached 539GW.

Wind Energy Systems

Fundamentally, a power wind energy system has two parts: mechanical and electric (see Figure 3). In the mechanical part, wind rotates a shaft to generate energy, whereas the electric one is responsible for transforming it into electricity suitable for the power grid. The two parts fit together in an electric generator, an electromechanical system that converts mechanical energy into electricity. Before feeding this electricity into the grid, it needs regulation by a power electronics converter, see Figure 3.

A transformer is used to boost the voltage level to that of the grid, enabling more efficient power transmission. Overall, wind energy becomes an easily regulated and controlled source of power.

Synchronisation

Grid synchronisation is an important aspect of connecting a grid-side converter (also known as grid-interactive inverter) to the grid. To operate in sync with the power grid, an algorithm is needed, called "synchronisation algorithm". To control the inverter, the phase angle of the grid voltage must be determined continuously and accurately.

Figure 4 shows the grid-synchronisation block diagram for a wind-energy system. The phase voltages of the grid are measured by sensors, and the synchronisation algorithm determines their phase angles. The detected phase angle is then exported to a digital controller, which controls the inverter, keeping it synchronised with the power grid.

Conventional and Fuzzy-Based PLL Algorithms

Phase locked loop (PLL) algorithms are widely used in three-phase on-grid systems for grid synchronisation because they are simple, easy to implement and perform well.

The PLL operates as a feedback system to instantaneously detect the phase angle (θ) of the grid voltages. Figure 5 shows a basic block diagram of a conventional PLL.

In a PLL system, the measured three-phase grid voltages (V_a, V_b and V_c) are first converted into rotating-axis variables (V_d and V_q), which are DC components.

Under ideal grid conditions, the determined phase angle (θ*) is equal to the phase angle of the grid (θ) and, as can be seen from the equations below, if V_q is zero, V_d is equal to the peak value of the grid voltage; V_q includes information about the grid's phase angle error, and V_d gives the amplitude information of the grid voltage in steady state.

$$V_q = V_m \sin(\theta - \theta^*); \quad V_d = V_m \cos(\theta - \theta^*)$$

In the control algorithm of the PLL, it is very important that the obtained phase angle be locked fast to the phase angle of the grid, and that it has good filtering characteristics matching the system's dynamic range. A proportional integral (PI) controller is normally used for PLL control. It also operates as a loop filter in the system, which controls the V_q voltage and determines the system's dynamics. Under non-ideal grid conditions such as an unbalanced or distorted grid, setting the PI coefficients (K_p and K_I) keep the system stable. But, in different imbalance and distortion situations, the phase angle (θ*) can be incorrectly calculated for the same K_p and K_I values. Furthermore, even if these two are updated according to the variable conditions, the phase angle is still improperly estimated and synchronisation time increases.

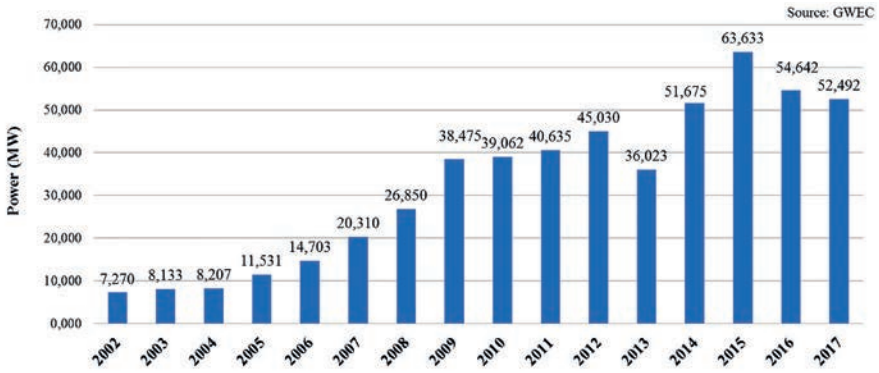

Figure 1: Annual installed global wind power capacity 2002-2017

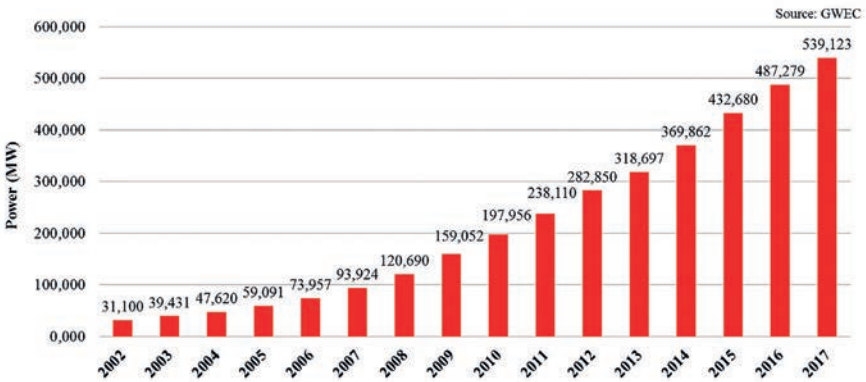

Figure 2: Cumulative installed global wind power capacity 2002-2017

To improve the dynamic response of the conventional PLL and estimate the phase angle quickly and accurately under non-ideal grid conditions, it is necessary to use an adaptive control algorithm. In this study, we use a fuzzy logic controller (FLC) instead of a PI controller; see Figure 6. In addition, we added a low-pass filter (LPF) to obtain a mean value of V_d ($\overline{V_d}$) very close to the real V_d value. In this context, using an FLC is more convenient than a PI controller, since FLC has a non-linear, adaptive control mechanism and robust performance in various conditions, and is one of the more intelligent control algorithms. Thanks to its non-linear and adaptive structure, FLC is suitable for grid conditions where changes can occur, including unbalanced and distorted grid conditions.

Simulation Results

We tested the PI-controlled classical PLL method and a simulated fuzzy-controlled PLL method under two different grid conditions – unbalanced and distorted. In the conventional PLL method, we calculated the PI coefficients $K_p = 0.74$ and $K_I = 85.05$, taking into account that the damping ratio of the PLL loop filter is $\xi = 0.707$, the natural frequency is $\omega_n = 162.63$rad/s and the settling time is two periods, or 40ms.

In fuzzy PLL, we determined the V_q error and the variation of the V_q error (derivative) as input variables, and designed the angular frequency variation of the grid ($\Delta\omega$) as output variable. Furthermore, we expressed each input and output variable with a 7-triangular membership function, using the Mamdani-type fuzzy inference mechanism.

As shown in Figure 7, we set the three-phase grid voltages to a peak value of 311V and the grid frequency at 50Hz for a 0-0.1s time interval under a balanced grid condition, and we didn't include a phase error for either method. Following that, we tested the PLL methods under an unbalanced grid condition of 0.1-0.2s (as unbalanced grid voltages we applied 373V peak value for the A phase, and 285V peak value for the B and C phases).

A big phase error shows in the test in the PI-controlled PLL (max phase error = 0.081rad, i.e. 4.64°), and a very small error in the fuzzy-controlled PLL (max phase error = 0.0012rad, i.e. 0.069°).

In the last setup, i.e. a distorted grid condition, we added the 5th and 7th harmonic components to the grid voltages. The amplitude of 5th harmonic component is 10% for each grid phase voltage (31V) and 5% (15.5V) for the 7th harmonic component. In the final test, we received fewer errors for each PLL compared to the previous condition; however, while the maximum phase error was 0.021rad (1.2°) in the PI-controlled PLL, for the fuzzy one it was 0.0002rad (0.011°); see a summary of the test results in Table 1. >

Grid Conditions	PI-PLL	Fuzzy-PLL
Balanced	0rad	0rad
Unbalanced	0.081rad (4.64°)	0.0012rad (0.069°)
Distorted	0.021rad (1.2°)	0.0002rad (0.011°)

Table 1: Comparison of PLL methods according to grid conditions

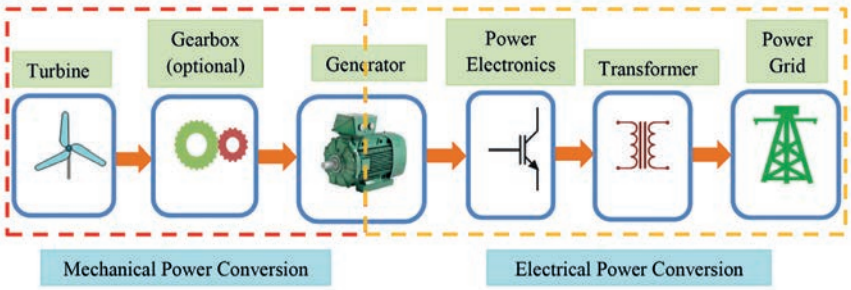

Figure 3: The path from wind to wall

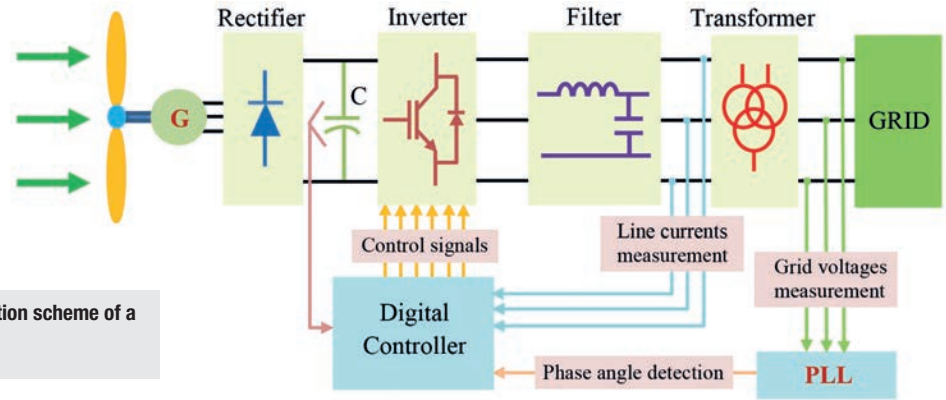

Figure 4: Grid synchronisation scheme of a wind energy system

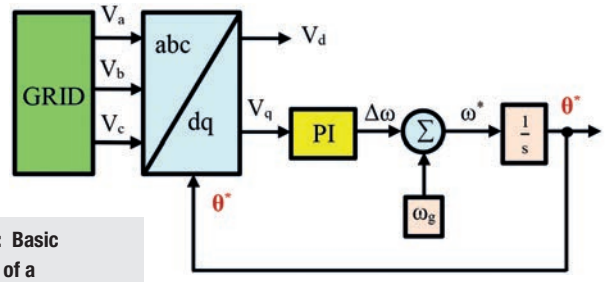

Figure 5: Basic diagram of a conventional PLL system

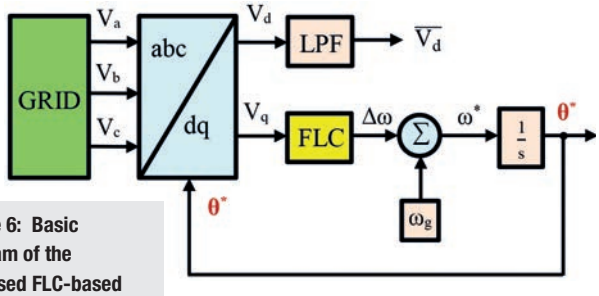

Figure 6: Basic diagram of the proposed FLC-based PLL system

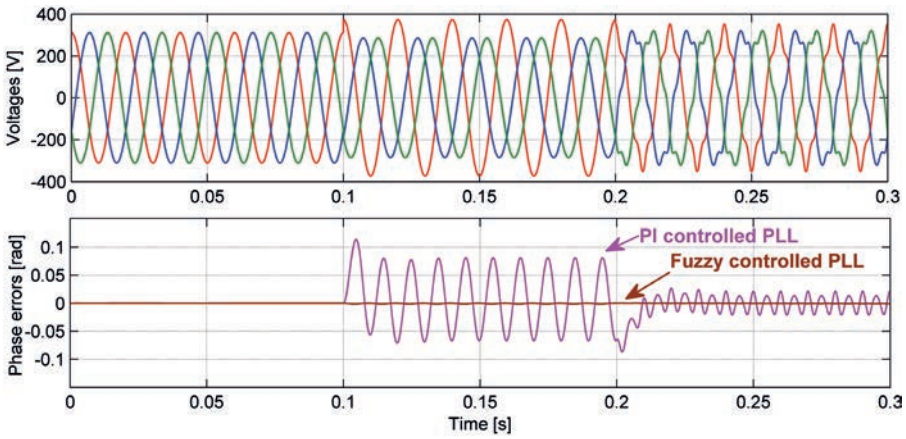

Figure 7: Grid voltage and phase error variations for PI- and fuzzy-controlled PLL

Significant Improvements

In our study we improved the performance of the conventional PLL under unbalanced and distorted grid conditions. Table 1 shows that the PI-controlled PLL can't be adapted to unbalanced or distorted grid conditions, which causes a big fault when determining the grid's phase angle. On the other hand, it's clear that the FLC-controlled PLL is very well adapted to these adverse grid conditions, and that the phase angle is determined almost without error. Consequently, comparative results show that the fuzzy-controlled PLL determines the grid phase angle more quickly and more precisely by means of the adaptive nature of the FLC. EW

Resonator-based metamaterial sensor for detecting unknown materials

By Md. Naimur Rahman and Mohammad Tariqul Islam, Universiti Kebangsaan Malaysia, and Md. Samsuzzaman, Patuakhali Science and Technology University, Bangladesh

Figure 1: Top (a) and bottom (b) of the metamaterial's layout

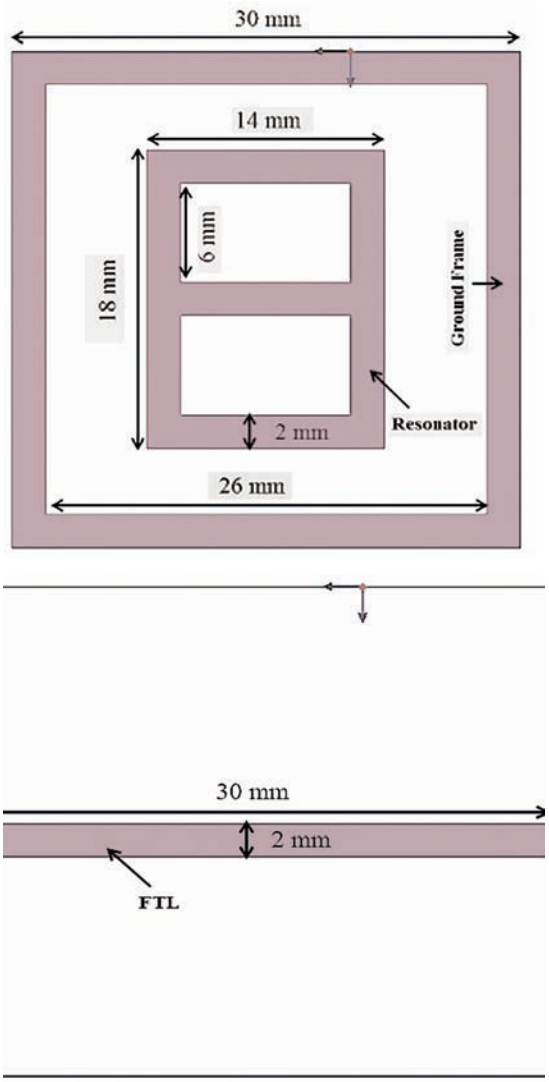

Manmade composite materials with properties not usually found in nature, such as a negative refractive index for example, are called metamaterials. They were first introduced by Russian physicist Victor Veselago in 1968, but have since become a field of increased research, especially specific characteristics such as negative permeability and negative permittivity.

Over the years, researchers have suggested many resonator-based metamaterials for different operating frequencies. Such metamaterials find many applications, including microwave imaging, terahertz sensing, sensors, absorbers and many more. In this article, we propose a metamaterial based on a resonator shaped as a figure of eight (8), because of its simplicity and ease of fabrication. The proposed structure is based on microstrip technology, for sensor applications in the GHz operating band.

Design Analysis and Measurement

In our study, the resonator and a ground frame were used along with a feedback transmission line (FTL) to create the metamaterial. The structure was designed on a 1.6mm-thick low-cost FR4 dielectric substrate, with relative permittivity of 4.6 and a loss tangent of 0.02.

The resonator and ground frame are etched on the same side of the substrate, with the FTL placed on the opposite; see Figure 1. The metamaterial structure is simulated and analysed with a High-Frequency Structural Simulator (HFSS). Excitation to the resonator was supplied through the FTL. We built the metamaterial structure on a printed circuit board using the circuit plotter LPKF, S63; see Figure 2. For the measurements we used the N5227A PNA Microwave Network Analyser (10MHz-67GHz).

Figure 3 shows this metamaterial's reflection and transmission coefficients. The resonances are found at 3GHz and 6.5GHz, where reflections are minimal and transmissions maximum. In the measurement, the transmission resonance frequency is found at 6.0GHz. Although there's little disagreement between the reflection and transmission coefficients of the simulated and measured results, they are uniform over the entire operating band. Disagreement between simulated and measured results occurs due to fabrication tolerances, soldering inaccuracies and external reflections.

Metamaterial Sensor Application

The proposed resonator-based metamaterial structure is used for a double-sided sensing system, where both front and back are used. The material to be detected is used as an over-layer. By changing the thickness and dielectric constant of the unknown material, the frequency response of the metamaterial sensing device varies.

First, we changed the over-layer's thickness. For the simulations we used an over-layer with dielectric constant of 4.4 and a 0.025 loss tangent, since these parameters are very close to those of the FR4 substrate used in our metamaterial; see Figure 4a. The figure shows that the transmission resonance shifts downward with increased over-layer thickness.

The sensing device along with the over-layer can be considered an RLC resonant circuit, where the resonance frequency is calculated by the effective capacitance and inductance. With increased thickness, the effective inductance and capacitance change, shifting the transmission resonance downward. Thus, the proposed metamaterial structure can be used effectively in sensing applications for the GHz region.

We also analysed the frequency response in reaction to varying the over-layer's relative permittivity; see Figure 4b. We found that when the relative permittivity increases, the transmission resonance downshifts too. Higher over-layer permittivity corresponds to a larger downshift of transmission resonance, increasing the metamaterial's sensitivity.

To validate the simulation, we used the FR4 material with relative permittivity of 4.6 and a 0.02 loss tangent, and the Rogers RO4350 material with relative permittivity of 3.66 and a 0.004 loss tangent. The respective materials' thicknesses were 1.60mm and 1.53mm; see Figure 5.

In Figure 6, the resonance frequency shifts downward with the over-layers' increasing thickness and relative permittivity. As the FR4 is thicker and with higher relative permittivity than the Rogers RO4350 material, FR4 shifts more downward than the Rogers RO4350 over-layer with reference to no over-layers, which is shown in Figure 3. More specifically, with no over-layer, the transmission resonance is 6.0GHz, but using the Rogers RO4350 and FR4 over-layers, the transmission resonance shifts to 5.0GHz and 4.8GHz, respectively.

We also considered double over-layer structures, using FR4+FR4 and Rogers RO4350+Rogers RO4350 substrates; see Figure 7 for the simulated and measured frequency responses. The figure shows that the resonance frequency shifts downward with increased over-layer thickness and relative permittivity. With no over-layer, the transmission resonance is 6.0GHz, but using the Rogers RO4350+Rogers RO4350 and FR4+FR4 double over-layers, the transmission resonance shifts to 4.6GHz and 4.3GHz, respectively.

Based on simulations and measurements, it is confirmed that the proposed resonator-based metamaterial can detect materials with different thicknesses and relative permittivities, making it suitable as a sensor for detecting unknown materials. EW

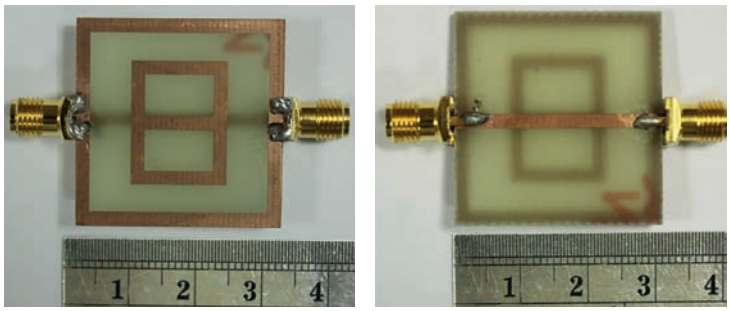

Figure 2 Top (a) and bottom (b) of the metamaterial prototype

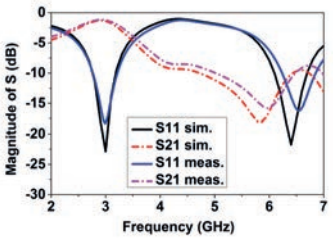

Figure 3: Simulated and measured magnitude of the S-parameter

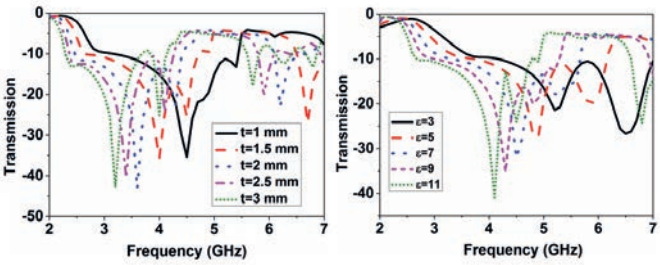

Figure 4: Over-layer thickness (a) and permittivity (b) with change of transmission

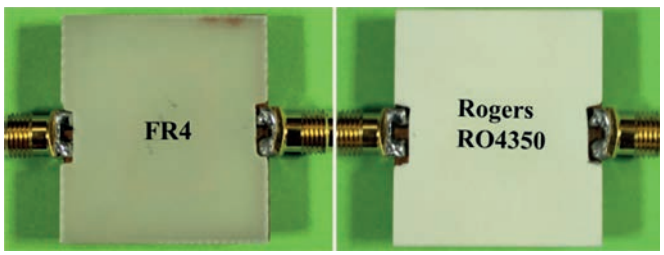

Figure 5: FR4 (a) and Rogers RO4350 (b) as over-layer in the sensing device

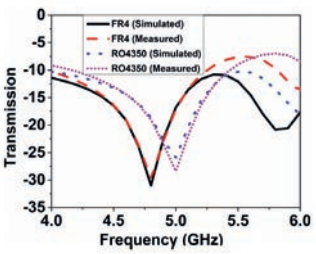

Figure 6: Simulated and measured transmission response with FR4 and Rogers RO4350 as over-layers

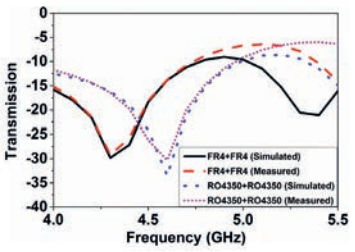

Figure 7: Simulated and measured transmission responses with FR4+FR4 and Rogers RO4350+Rogers RO4350 double over-layers

New T model incorporating conductor and substrate parasitic losses for on-chip transformers

By Minglin Ma, Yuan Chen, Zhijun Li, Xue Zhang and Xiangliang Jin,
Xiangtan University, China

The demand for low-power, low-cost and high-integration wireless communication systems is driving the development of on-chip passive devices for radio frequency integrated circuits (RFICs).

Among the passive circuit designs, on-chip spiral transformers are particularly important and widely used in RFICs, including mixers, low-noise amplifiers, power amplifiers and oscillators. This calls for accurate lumped-element models for on-chip transformers, suitable for circuit simulation and design optimisation. Modelling the transformer and obtaining its parameters are always of great concern for engineers and circuit designers.

Several compact transformer models and circuit parameter-determining approaches have been proposed over the years, including a double π model that has 42 components and expressions for spiral transformers; an automatic parameter determination and scaleable modelling method; and a generalised four-port transformer model with an ideal transformer at its core.

Commonly-used transformer model specifications don't include high-order effects with increasing frequency, which can result in underestimated power consumption of the circuit model when compared to the actual transformer's performance.

Certain physics-based modelling methods for calculating the transformer model parameters from geometry, and the necessary semiconductor process have also been developed. However, these process parameters are not always well defined for modelling purposes. In addition, some expressions are merely empirical formulas that depend on a specific fabrication process. Thus, some of the models' parameters are totally or partially determined by fitting and optimisation procedures.

We propose a new T-lumped-element circuit model for circle-shaped planar transformers. This model accurately captures conductor losses in the transformer windings as well as substrate parasitic losses over a broad frequency range. The values of the T-lumped elements of the circuit model are determined from two-port S-parameter data obtained from measurements.

This model accurately captures conductor losses in the transformer windings

Model Development

Figure 1 shows the proposed corresponding physics-based equivalent circuit model for on-chip spiral transformers. Here, R_{i0} (i = p, s) is introduced to account for the spiral coil's resistive loss, and C_{i0} (i = p, s) is the coupling capacitance between adjacent metal tracks and the overlap capacitance between the spiral and underpass metal lines. Direct current is uniformly distributed inside the conductor, characterised by R_i and L_i (i = p, s). As the frequency goes up, skin and proximity effects will push the

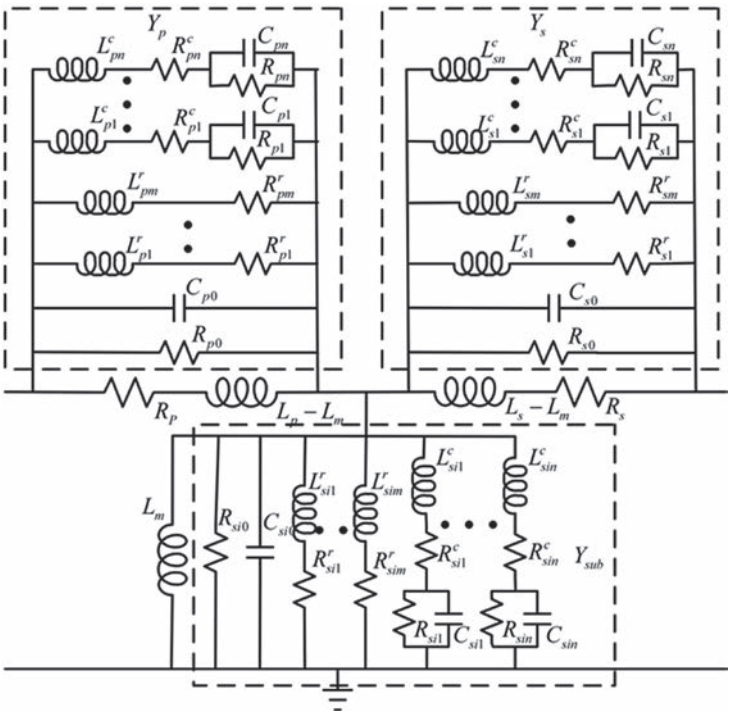

Figure 1: New compact model for transformers

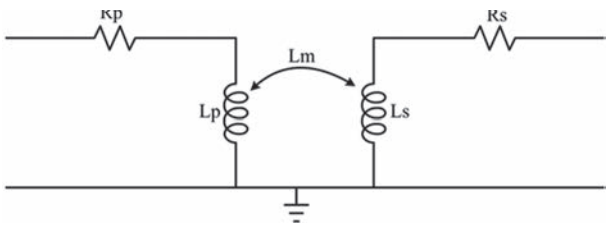

Figure 2: Physical model for low-frequency bands

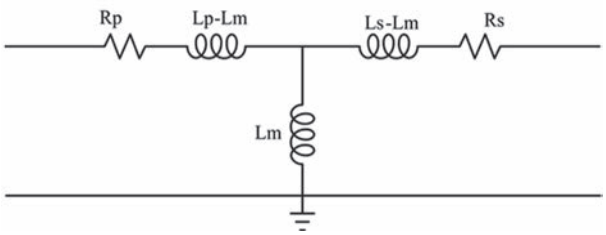

Figure 3: Decoupling conversion

alternating current to the surface of the metal, requiring an additional L_R and L_{RC} ladder in parallel with R_i and L_i to capture the different current densities in the conductor.

The conventional substrate parasitic can be modelled by C_{ox}, C_{sub} and R_{sub}, with C_{ox} representing the metal-oxide capacitance and C_{sub} and R_{sub} the substrate capacitance and resistance. But, for substrate high-order effects such as the eddy effect, characterising the capacitive and resistive couplings alone is not enough.

A new block shown as Y_{sub} in Figure 1 was introduced to model substrate parasitic losses, where R_{si0} is the substrate resistance, C_{si0} the capacitance of the metal-oxide and substrate, and an LR and LRC series branch accounts for the model's high-order effects. This block significantly improves the accuracy of the model. More branches will describe the high-order effects more accurately.

The magnetic couplings between the two coils are represented by L_m.

For convenience, the portions including R_{i0}, C_{i0}, L_R and L_{RC} in the series branch of the equivalent circuit will be denoted by Y_i (i = p, s), and the sections including C_{si0}, R_{si0}, L_R and L_{RC} in the shunt branch by Y_{sub}, as indicated by the dashed lines in Figure 1.

Parameter Determination

In low-frequency bands, the physical transformer model can be described as in Figure 2. Here R_i and L_i (i = p, s) denote the DC resistance and inductance of the corresponding coil, respectively; L_m is introduced to account for the mutual inductance between the primary and secondary coils. We can easily convert this π topology to the T topology and determine R_i, L_i (i = p, s) and L_m with:

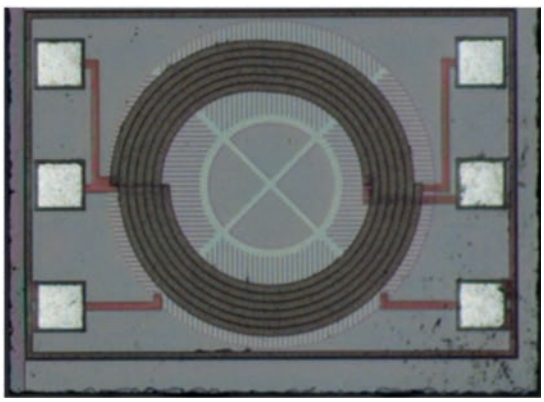

Figure 4: Top view of the fabricated on-chip transformer

$$L_m = \left.\frac{im\left[(Z_{12}+Z_{21})/2\right]}{w}\right|_{w\to 0} \quad (1)$$

$$R_i = re(Z_{ii}-Z_{12})\big|_{w\to 0}\,(i=p,s) \quad (2)$$

$$L_i = L_m + \left.\frac{im(Z_{ii}-Z_{12})}{w}\right|_{w\to 0}\,(i=p,s) \quad (3)$$

The circuit parameter determination of the proposed model is mainly for Y_p, Y_s and Y_{sub}. When the elements L_p, R_p, L_s, R_s and L_m are determined, the Y_i (i = p, s) and Y_{sub} can be calculated with:

$$Y_i = \frac{1}{Z_{ii}-Z_{12}} - \frac{1}{R_i + jwL_i}\,(i=p,s) \quad (4)$$

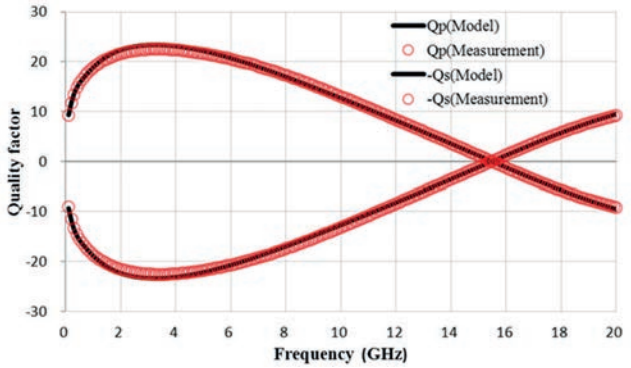

Figure 5: Quality factor comparisons

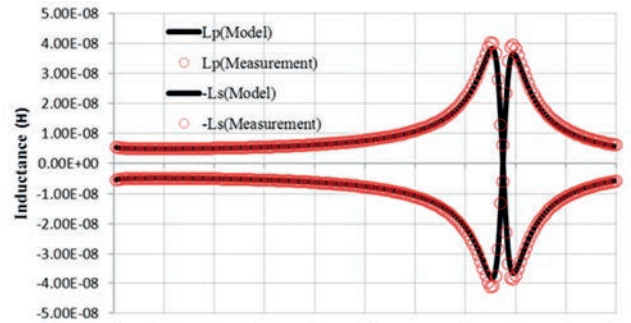

Figure 6: Inductance comparisons

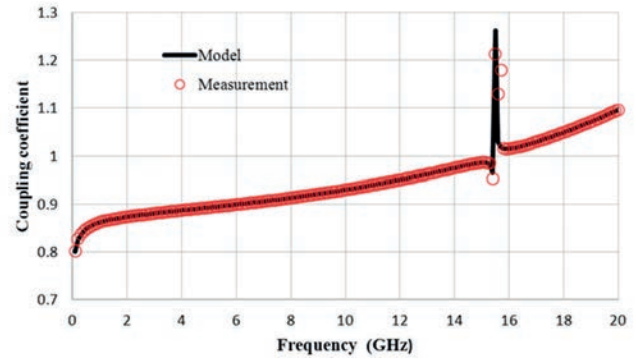

Figure 7: Coupling coefficient comparisons

$$Y_{sub} = \frac{2}{Z_{12}+Z_{21}} - \frac{1}{jwL_m} \tag{5}$$

Expanding the admittance of Y_i and Y_{sub} with the pole-residue formulation will implement the parameter determination process simply:

$$Y(s) = d + se + \sum_{i=1}^{m}\frac{r_i^r}{s-p_i^r} + \sum_{i=1}^{n}\frac{r_i^c}{s-p_i^c} + \frac{\tilde{r}_i^c}{s-\tilde{p}_i^c} \tag{6}$$
$$= d + se + \sum_{i=1}^{m}\frac{r_i}{s-p_i} + \sum_{i=1}^{n}\frac{\lambda_i s+\gamma_i}{s^2+\alpha_i s+\beta_i}$$

In Equation 6, d, e, r_i, p_i, α_i, β_i, γ_i and λ_i are real, with the rest complex. To synthesise a lumped equivalent circuit by Y(s), Y_j (j = p, s, si) is expressed by R, L, C as:

$$Y_j(s) = \frac{1}{R_{j0}} + sC_{j0} + \sum_{i=1}^{m}\frac{1/L_{ji}^r}{s+R_{ji}^r/L_{ji}^r} + \sum_{i=1}^{n}\frac{(1+L_{ji}^c)s+1/L_{ji}^c C_{ji}R_{ji}}{s^2+(R_{ji}^c/L_{ji}^c+1/C_{ji}R_{ji})s+(1+R_{ji}^c/R_{ji})/(L_{ji}^c C_{ji})} \tag{7}$$

The superscripts r and c stand for real and complex poles. The order of real and complex poles are m and n. Compared with the aforementioned Y(s), the R, L, C components of the circuit in Figure 1 can be determined with:

$$\left.\begin{aligned} R_{j0} &= 1/d \\ C_{j0} &= e \end{aligned}\right\}(j = p,s,si) \tag{8}$$

$$\left.\begin{aligned} L_{ji}^r &= 1/r_i^r \\ R_{ji}^r &= -p_i^r/r_i^r \end{aligned}\right\}(j = p,s,si;i = 1\cdots m) \tag{9}$$

$$\left.\begin{aligned} L_{ji}^c &= 1/\lambda_i \\ R_{ji}^c &= L_{ji}^c(\alpha_i - L_{ji}\gamma_i) \\ R_{ji} &= \beta_i/\gamma_i - R_{ji}^c \\ C_{ji} &= 1/L_{ji}^c R_{ji}\gamma_i \end{aligned}\right\}(j = p,s,si,i = 1\cdots n) \tag{10}$$

Therefore, all the elements in Y_p, Y_s and Y_{sub} are identified. This parameter-determining method has been implemented in the MATLAB environment using the VF (vector fitting) method.

Parameter	Value	Parameter	Value
R_p, R_s/Ω	62	L_m/nH	4.26
L_p, L_s/nH	2.6	R_{si0}/kΩ	1.28
C_{p0}, C_{s0}/fF	3.56	C_{si0}/fF	27.8
R_{p0}, R_{s0}/Ω	667	L_{si1}^r/nH	260
L_{p1}^r, L_{s1}^r/nH	2.37	R_{si1}^r/Ω	203
R_{p1}^r, R_{s1}^r/Ω	11.5	L_{si2}^r/nH	212
L_{p2}^r, L_{s2}^r/nH	2.12	R_{si2}^r/kΩ	1.15
R_{p2}^r, R_{s2}^r/Ω	2.15	L_{si3}^r/nH	2.4
L_{p3}^r, L_{s3}^r/nH	1.55	R_{si3}^r/kΩ	1.04
R_{p3}^r, R_{s3}^r/Ω	0.16	L_{si1}^c/uH	9.53
L_{p1}^c, L_{s1}^c/nH	2.61	R_{si1}^c/kΩ	0.29
R_{p1}^c, R_{s1}^c/Ω	4.93	R_{si1}/kΩ	2.27e4
R_{p1}, R_{s1}/kΩ	299	C_{si1}/fF	1.47
C_{p1}, C_{s1}/fF	1.77		

Table 1: The determined model parameters

Model Verification

To verify the model's performance, an on-chip interleaved transformer with PGS (patterned ground shield) has been fabricated in a 0.5µm L50G CMOS process; the line width and spacing are 10 and 2µm respectively, and the transformer's inner diameter is 130µm, as shown in Figure 4. The measured S-parameter is extracted with a two-step (open and short) procedure to remove the undesired pad parasitics.

We used Z parameters converted from the measured S-parameters to determine the self-inductance (L_p and L_s), quality factors (Q_p and Q_s) and coupling coefficient (k) as functions of frequency. These are calculated using the following expressions:

$$L_p = \frac{im(Z_{11})}{2\pi f} \quad (11)$$

$$L_s = \frac{im(Z_{22})}{2\pi f} \quad (12)$$

$$Q_P = \frac{im(Z_{11})}{re(Z_{11})} \quad (13)$$

$$Q_S = \frac{im(Z_{22})}{re(Z_{22})} \quad (14)$$

$$k = \sqrt{\frac{im(Z_{12})im(Z_{21})}{im(Z_{11})im(Z_{22})}} \quad (15)$$

To verify the procedure's efficiency and accuracy, we have compared the modelled and measured L_p, L_s, Q_p, Q_s and k. It only takes four parallel branches (three branches for real poles and one for complex poles) to represent the high-order effects. The model parameters generated by the direct determination procedure are listed in Table 1.

For clarity in Figures 5 and 6, we compared the curves of $-L_s$ and $-Q_s$ instead of L_s and Q_s. RMS deviations of the simulated Q_p and Q_s in Figure 5 are below 2.59%, the simulated L_p and L_s in Figure 6 are below 6.89%, and the simulated k value in Figure 7 is 7.61%.

The frequency range chosen for the RMS calculation is between 0.1GHz and 20GHz. The relative deviation is below 1.13% for the DC inductance L, and below 3.47% for the peak value of Q. As demonstrated in these three figures and deviations, an excellent agreement has been found over a broad frequency range; hence, the model in Figure 1 is accurate enough to model the transformer, with the parameter-determining procedure showing high efficiency and accuracy without any optimisation.

The equivalent circuit model is compatible with common circuit simulators such as SPICE, for transient and frequency domain simulation. EW

Integrated bidirectional bridge with dual RMS detectors for RF power and return-loss measurement

By Eamon Nash, applications engineering director, and Eberhard Brunner, senior design engineer, Analog Devices

Directional couplers are used in many applications to sense RF power, and may appear at multiple points in a signal chain. Inline RF power and return loss measurements are typically implemented using directional couplers and RF power detectors.

In Figure 1, a bidirectional coupler is used in a radio or test and measurement application to monitor transmitted and reflected RF power. It's also sometimes desirable to have RF power monitoring embedded in a circuit, a good example being when two or more sources are switched into the transmission path, either using an RF switch or external cables.

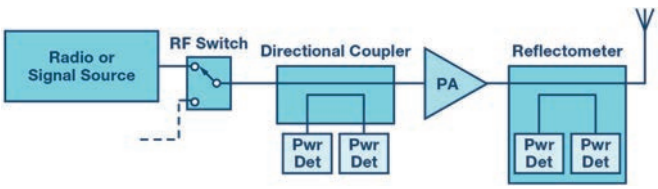

Figure 1: Measuring forward and reflected power in an RF signal chain

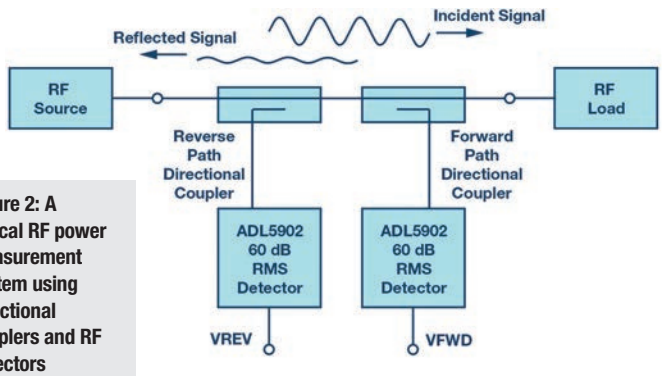

Figure 2: A typical RF power measurement system using directional couplers and RF detectors

Directional couplers have the valuable characteristic of directivity, which is the ability to distinguish between incident and reflected RF power. As the incident RF signal travels through the forward-path coupler on its way to the load (Figure 2), a small portion of the RF power – usually 10-20dB lower than the incident signal – is coupled away to drive an RF detector. Where both forward and reflected power are being measured, a second coupler is used with reverse orientation compared to the forward coupler. The output voltages from the two detectors will be proportional to the forward and reverse RF power levels.

Surface-mount directional couplers suffer from a fundamental tradeoff between bandwidth and size. While bidirectional directional couplers with one octave of frequency coverage (F_{MAX} is equal to twice F_{MIN}) are commonly available in packages as small as 6mm^2, a multi-octave surface-mount directional coupler will be

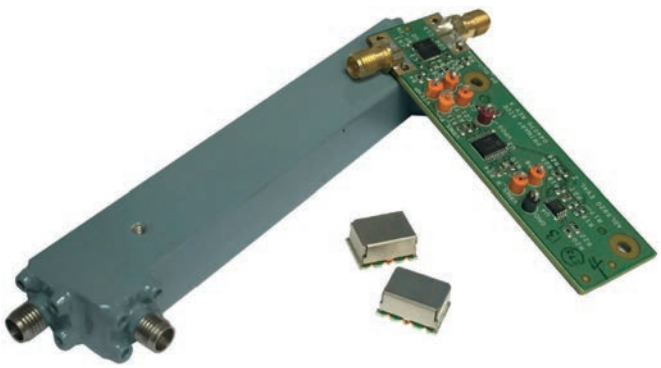

Figure 3: A connectorised directional coupler, surface-mount directional coupler and ADL5920 integrated IC with directional bridge and dual rms detectors

much larger; see Figure 3. Broadband connectorised directional couplers have multioctave frequency coverage but are significantly larger than surface-mount devices.

Figure 3 also shows the evaluation board for the ADL5920 (Figure 4), a new RF power detection subsystem from Analog Devices, with detection range up to 60dB, packaged in a 5mm × 5mm MLF package (the ADL5920 IC shown is located between the RF connectors).

Instead of sensing the forward and reflected signals using directional couplers, the ADL5920 uses a patented directional bridge technology to achieve broadband and compact on-chip signal coupling. To understand how a directional bridge works, we first need to look at the Wheatstone bridge.

Wheatstone Bridge

The notion of a directional bridge is based on the Wheatstone bridge (Figure 5), which creates zero differential voltage when balanced. In it, one of its legs' resistors is variable (R_2), with the two others (R_1 and R_3) fixed.

There are four resistors in total (R_1, R_2, R_3, R_x), where R_x is an unknown resistance. If $R_1 = R_3$ and R_2 is equal to R_x, then V_{OUT} = 0V. The bridge is considered balanced when the variable resistor is of a value such that the voltage-divide ratios on the left and right side of the bridge are equal and thereby create a zero-volt differential signal across the differential sense nodes that produce V_{OUT}.

A Unidirectional Bridge

Figure 6 shows the schematic of a unidirectional bridge, and it best explains the basic operation of such a device. First, it is important to observe that a directional bridge needs to be designed for a specific Z_0 so that insertion loss is minimised. If $R_S = R_L = R = 50\Omega$, then the sense resistor of the bridge is 5Ω, a good compromise between insertion loss (< 1dB) and signal sensing.

Calculating R_{OUT} as seen looking back from the load results in an exact 50Ω port impedance while calculating R_{IN} will result in 50.8Ω port impedance ($|\Gamma| = 0.008$; RL = -42dB; VSWR = 1.016). If a signal is applied as shown at the RFIP node, since $R_{IN} \sim 50\Omega$, the voltage at RFIP is about half the source voltage. If we assume for a moment that the voltage at RFIP is 1V, then the voltage at RFOP will be about 0.902V. This voltage is further attenuated by 10/11 = 0.909 such that the negative input of the differencing amplifier is 0.82V with a resultant differential voltage of (1 – 0.82) = 0.18V. The effective forward coupling factor (Cpl) of this bridge is:

$$Cpl = 20log_{10}\left(\frac{0.18\ V}{1\ V}\right) = 15\ dB \quad (1)$$

'Balanced' in the context of the bridge means that when a signal is applied in the reverse direction (RFOP to RFIP), then the V_{FWD} detector (or Cpl port) will ideally see zero differential voltage, while

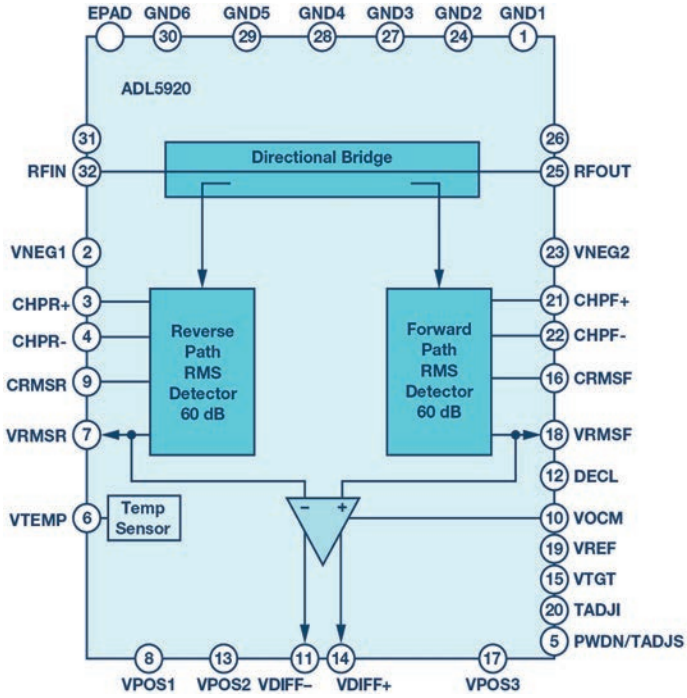

Figure 4: ADL5920 block diagram

it sees a maximum signal when the signal is applied in the forward direction (RFIP to RFOP). To get maximum directivity in such a structure, precision resistors are of utmost importance, which is why integrating them is beneficial.

In a unidirectional bridge, to determine isolation, which is needed to calculate return loss (RL), one needs to flip the device and apply the input signal to RFOP. In this case, the bridge is balanced and the plus and minus inputs to the differential amplifier are equal, since the same divide-ratios of 0.909 = [10R/(10R + R) = (R/(R+0.1R)] result in a differential voltage of (V+ minus V–) = 0V.

Bidirectional Bridge

Figure 7 shows a simplified diagram of a bidirect-ional bridge, like the one used in the ADL5920. The unit resistance R is equal to 50Ω for a 50Ω environment. So, the value of the bridge's sense resistor is 5Ω, while the two shunt networks are about 1.1kΩ each. This is a symmetric network, so the input and output resistances, R_{IN} and R_{OUT}, are the same and close to 50Ω when R_S and R_L are also equal to 50Ω.

When the source and load impedance are both 50Ω, an ohmic analysis of the internal network tells us that V_{FWD} will be quite large compared to V_{REV}. In a real-world application, this corresponds to maximum power transmission from source to load. This results in little reflected power, which in turn results in a very small V_{REV}.

Next, let's consider what happens if R_L is either infinite (open-circuit) or zero (shorted load). In both cases, repeating the ohmic analysis, we find that V_{FWD} and V_{REV} are approximately equal. This

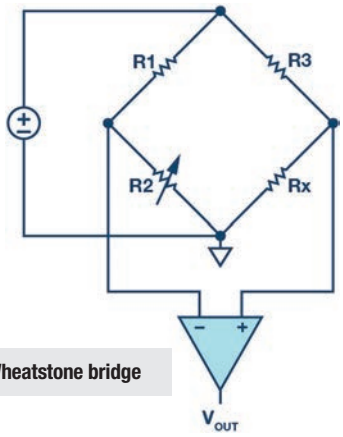

Figure 5: Wheatstone bridge

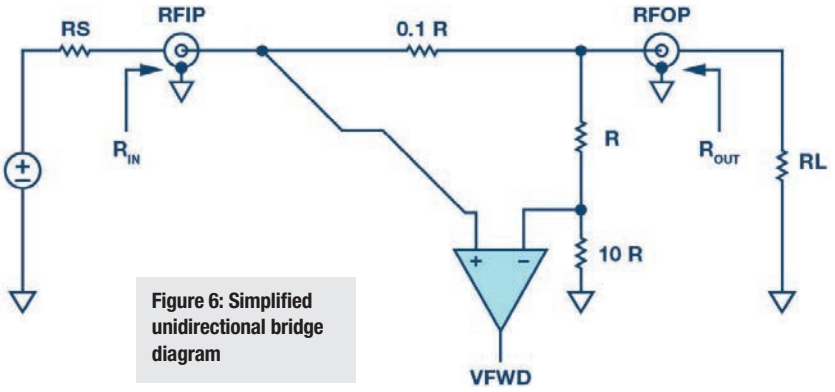

Figure 6: Simplified unidirectional bridge diagram

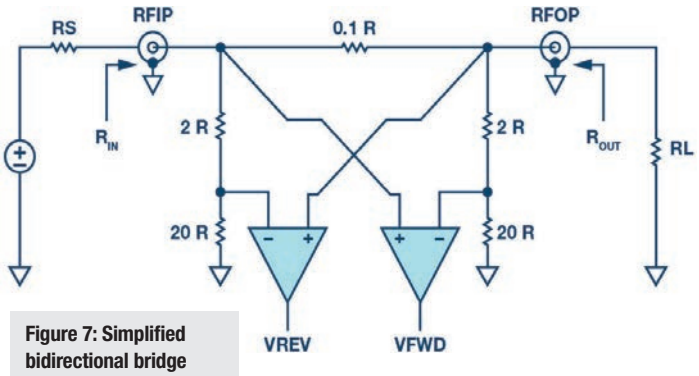

Figure 7: Simplified bidirectional bridge diagram

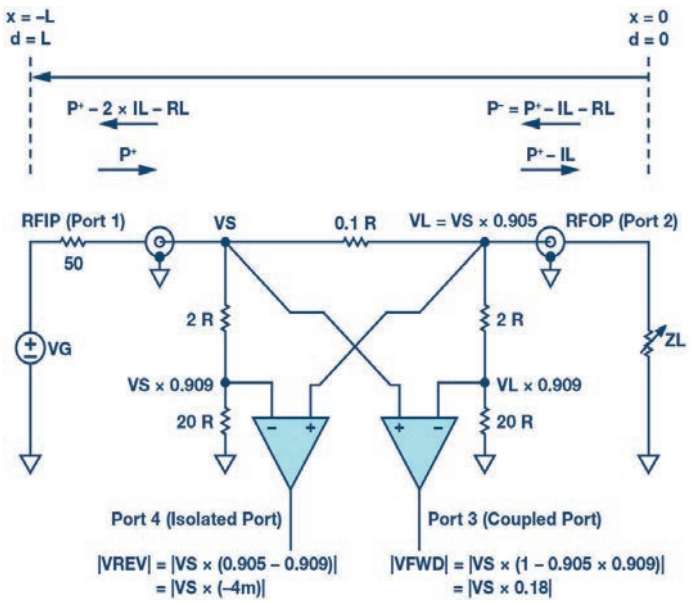

Figure 8: Simplified bidirectional bridge with signals

mirrors a real-world system where an open- or shorted-load results in equal forward and reflected power. A more detailed analysis of these scenarios follows below.

VSWR and Reflection Coefficient

A full analysis of errors in network analysis is complicated and beyond the scope of this article, but we will summarise some of the basic concepts here. An excellent resource is the application note by Marki Microwave, 'Directivity and VSWR Measurements', easily found online.

Travelling waves are an important concept to describe the voltages and currents along transmission lines, since they are functions of position and time. The general solution of voltages and currents along transmission lines consist of a forward-travelling wave and a reverse-travelling wave; both are functions of distance x:

$$V(x) = V^{+}(x) + V^{-}(x) \quad (2)$$

$$I(x) = \frac{V^{+}(x)}{Z_0} - \frac{V^{-}(x)}{Z_0} \quad (3)$$

In Equations 2 and 3, V+(x) represents the voltage wave travelling toward the load, while V–(x) represents the voltage wave reflected from the load due to mismatch. Z_0 is the characteristic impedance of the transmission line, and in a lossless transmission line, it is defined by the classic equation:

$$Z_0 = \sqrt{\frac{L}{C}} \quad (4)$$

The most common Z_0 is 50Ω for transmission lines. If such a line is terminated with its characteristic impedance, it appears to a 50Ω source as an infinite line, since any voltage wave travelling down the line will not result in reflections that can be sensed at the source or anywhere else along the line. However, if the load is other than 50Ω, then a standing wave that can be detected will be generated along the line, defined as the voltage standing wave ratio (VSWR).

More generally, the reflection coefficient is defined as:

$$\Gamma(x) = \Gamma_0 e^{2\gamma x} \quad (5)$$

where Γ_0 is the load reflection coefficient and γ the propagation constant of the transmission line.

$$\Gamma_0 = \frac{Z_L - Z_0}{Z_L + Z_0} \quad (6)$$

$$Z_0 = \sqrt{\frac{R + j\omega L}{G + j\omega C}} \quad (7)$$

$$\gamma = \sqrt{(R + j\omega L)(G + j\omega C)} \quad (8)$$

R, L, G and C are the resistance, inductance, conductance and capacitance per unit length of the transmission line. The return loss (RL) is the negative of the reflection coefficient (Γ) in dB. This is important to point out since reflection coefficient and return loss are frequently confused and used interchangeably.

$$RL = -20log_{10}|\Gamma_0| = 10log_{10}\frac{1}{|\Gamma_0|^2} \quad (9)$$

Another very important definition of return loss in addition to the load mismatch above is in terms of incident and reflected power at an impedance discontinuity. This is given by:

$$RL = 10log_{10}\left(\frac{P_{incident}}{P_{reflected}}\right) \quad (10)$$

and extensively used in antenna design. VSWR, RL and Γ_0 are related as follows:

$$|\Gamma_0| = \frac{VSWR - 1}{VSWR + 1} \quad (11)$$

$$VSWR = \frac{|V(x)|_{max}}{|V(x)|_{min}} + \frac{1 + |\Gamma_0|}{1 - |\Gamma_0|} = \frac{1 + 10^{\frac{RL}{-20}}}{1 - 10^{\frac{RL}{-20}}} \quad (12)$$

$$RL = -20log_{10}\left(\frac{VSWR - 1}{VSWR + 1}\right) \quad (13)$$

Equations 14 and 15 represent the maximum and minimum of the standing-wave voltages. VSWR is defined as the ratio of the maximum to the minimum voltage along the wave. The peak and minimum voltages along the line are:

$$|V(x)|_{max} = |A|(1 - |\Gamma_0|) \quad (14)$$

$$|V(x)|_{min} = |A|(1 - |\Gamma_0|) \quad (15)$$

For example, in a 50Ω transmission line, if the forward-travelling voltage signal has a peak amplitude of A = 1 and the line is matched with a perfect load, then $|\Gamma_0| = 0$, there is no standing wave (VSWR = 1.00), and the peak voltage along the line is A = 1. However, if

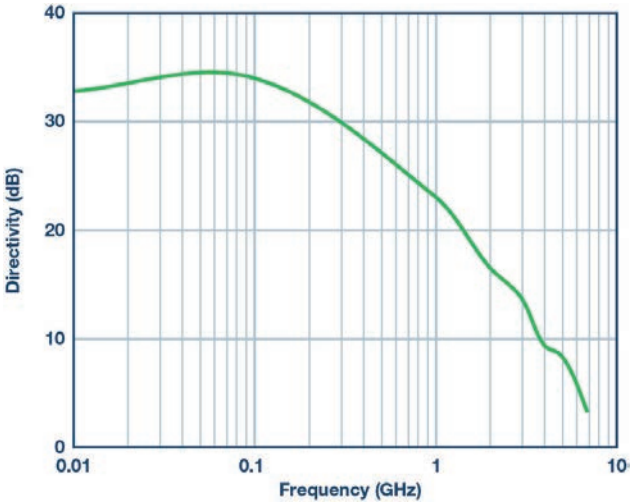

Figure 9: ADL5920 directivity vs frequency; the input level is 20dBm

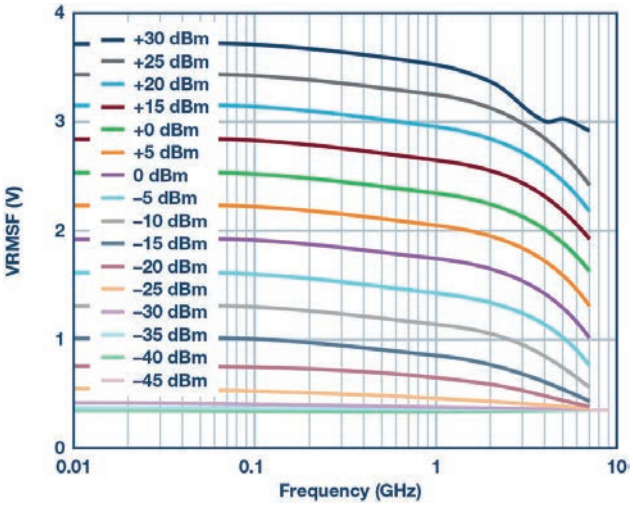

Figure 10: Typical output voltage vs frequency from forward path detector at multiple input power levels

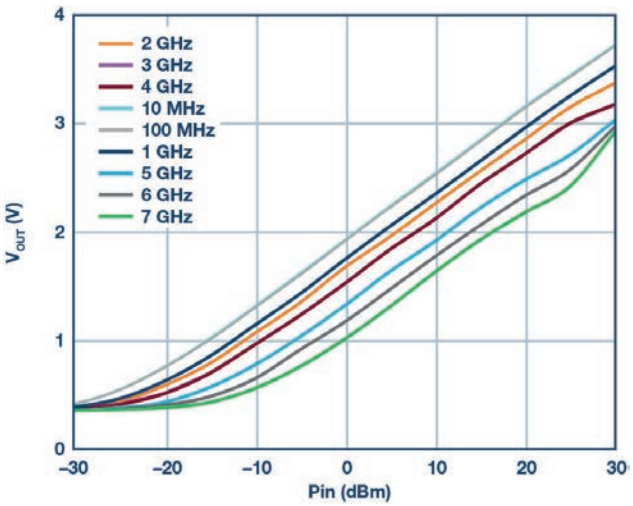

Figure 11: Typical output voltage vs input power from forward path detector at multiple frequencies

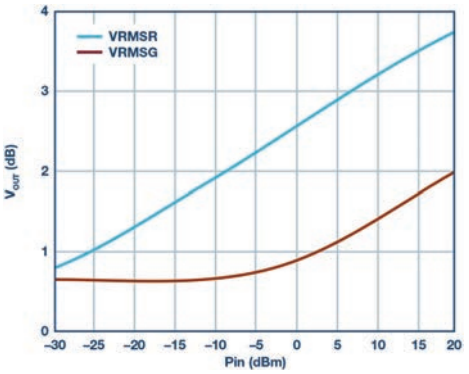

Figure 12: V_{RMSF} and V_{RMSR} output voltage vs input power at 500MHz when the bridge is driven from RF_{IN} and RF_{OUT} is terminated with 50Ω

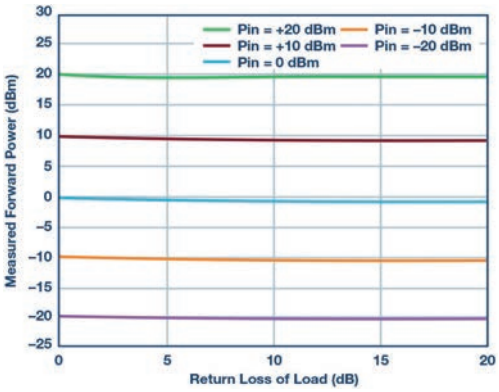

Figure 13: Measured forward power vs applied power and return loss of load, measured at 1GHz

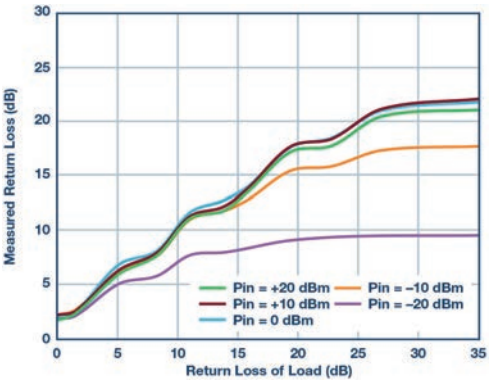

Figure 14: Measured return loss vs applied return loss and RF power, measured at 1GHz

R_{LOAD} is 100Ω or 25Ω, then $|\Gamma_0| = 0.333$, RL = 9.542dB and VSWR = 2.00, with $|V(x)|max = 1.333$ and $|V(x)|min = 0.666$.

Figure 8 is the same as Figure 7 but with signals shown in the default forward configuration and with travelling power waves shown where the reference plane is at the load. At low frequencies, where the wavelength is long relative to the physical structure, voltages and currents are in phase and the circuit can be analysed using Ohm's law.

The ports are defined as shown, with the input (Port 1) at RFIP, output (Port 2) at RFOP, coupled port (Port 3) at V_{FWD}, and isolated port (Port 4) at V_{REV}. Since the structure is symmetric, the ports are reversed when a signal is reflected at Z_L or applied to RFOP.

In the case of a matched load and generator voltage connected to Port 1 (RFIP), and with $Z_S = Z_L = Z_0 = R = 50\Omega$:

$$V_L = V_{S+}\left[\frac{Z_{OUT}}{Z_{OUT} + 0.1R}\right] = V_{S+} \times 0.905 = V_{S+} \times |S21| \quad (16)$$

$$Z_{OUT} = Z_L \,||\, (2R + 20R) = R \,||\, 22R = \left(\frac{22}{23}\right)R \quad (17)$$

and V_L/V_{S+} is the insertion loss, L_1, or IL in dB.

$$IL = -20log_{10}|S21| = -20log_{10}L_1 = 0.87\ dB \quad (18)$$

The attenuation factor α for the two shunt legs on either side of the main line resistor of 0.1 × R is:

$$\alpha = \frac{20R}{(20R + 2R)} = \frac{20}{22} = 0.909 \quad (19)$$

The equations in Figure 8 for $|V_{REV}|$ and $|V_{FWD}|$ show the values for those voltages with a signal applied in the forward direction. These equations indicate a fundamental directivity limit for the simplified schematic due to non-ideal rejection of 33dB at the isolated port.

$$D = 20log_{10}\left(\frac{|V_{CPL}|}{|V_{ISO}|}\right) = 20log_{10}\left(\frac{|0.18|}{|-0.004|}\right) = 33\ dB \quad (20)$$

Figure 8 shows that the directivity of the bidirect-ional bridge in the linear domain is determined by:

$$D_L = \left(\frac{1 - L_1 \times \alpha}{L_1 - \alpha}\right) \quad (21)$$

which means that to increase directivity, α needs to equal the insertion loss, L_1. In silicon, the peak directivity is typically better than the simplified diagram would indicate (Figure 9).

If Z_L is not equal to Z_0, as is normally the case, the coupled and isolated port voltages, which are complex, would be:

$$V_{CPL} = V_{S+}[1 - L_1 \times \alpha] + V_{L-}[L_1 - \alpha] \quad (22)$$

$$V_{ISO} = V_{L-}[1 - L_1 \times \alpha] + V_{S+}[L_1 - \alpha] \quad (23)$$

where V_{S+} is the forward voltage at Port 1 (node V_S) and V_{L-} is the reflected voltage from the load at Port 2 (node V_L). Θ is the unknown phase of the reflected signal:

$$V_{L-} = V_{S+} \times L_1 \times |\Gamma_0|e^{j\Theta} \quad (24)$$

Substituting Equation 24 for V_{L-} in Equations 22 and 23 and using Equation 21 to simplify the result, plus the fact that:

$$V_{FWD} = V_{S+}[1 - L_1 \times \alpha] \quad (25)$$

results in complex output voltages:

$$V_{CPL} = V_{FWD}\left\{1 + \frac{L_1 \times |\Gamma_0| e^{j\Theta}}{D_L}\right\} \quad (26)$$

$$V_{ISO} = V_{FWD}\left\{L_1 \times |\Gamma_0| e^{j\Theta} + \frac{1}{D_L}\right\} \quad (27)$$

From Equations 26 and 27 we can observe that for $D_L >> 1$:

$$\left|\frac{V_{ISO}}{V_{CPL}}\right|_{max,\ min} = \sqrt{\frac{\left(\frac{1}{D_L}\right)^2 \pm 2\left(\frac{L_1 \times |\Gamma_0|}{D_L}\right) + (L_1 \times |\Gamma_0|)^2}{1 + 2\left(\frac{L_1 \times |\Gamma_0|}{D_L}\right) + \left(\frac{L_1 \times |\Gamma_0|}{D_L}\right)^2}} \rightarrow L_1 \times |\Gamma_0| \quad (28)$$

In the ADL5920, the voltages V_{REV} and V_{FWD} are mapped via two 60dB-range linear-in-dB rms detectors into voltages V_{RMSR} and V_{RMSF} that are (V_{ISO}/V_{SLP}) and (V_{CPL}/V_{SLP}) in dB, respectively. So, the differential output of the device V_{DIFF} in dB represents:

$$\frac{V_{DIFF}}{V_{SLP}} = \frac{VRMSR - VRMSF}{V_{SLP}} = \frac{V_{L_1} + V_{|\Gamma_0|}}{V_{SLP}} \quad (29)$$

where V_{SLP}, the detector slope, is about 60mV/dB.

Using the voltage-to-dB mapping of Equation 29 in Equation 28:

$$20log_{10}\left(\frac{VRMSR}{V_{SLP}}\right) - 20log_{10}\left(\frac{VRMSF}{V_{SLP}}\right) = 20log_{10}(L_1) + 20log_{10}|\Gamma_0| \quad (30)$$

And using Equation 9 in Equation 30 gives:

$$P_{REV} - P_{FWD} = -IL - RL \quad (31)$$

$$RL = P_{FWD} - P_{REV} - IL \quad (32)$$

Figure 10 shows the response of the forward power-sensing rms detector when the ADL5920 is driven in the forward direction. Each trace corresponds to the output voltage vs frequency for a specific power level. While the plot stops at 10MHz, operation at frequencies to 9kHz has been verified. In Figure 11, the same data is presented as output voltage vs input power, with each trace representing a different frequency.

When the ADL5920's RF_{OUT} pin is terminated with a 50Ω resistor, there should be no reflected signal. Therefore, the reverse path detector should not register any detected reverse power. However, because the directivity of the circuit is non-ideal and rolls off with frequency, some signal will be detected in the reverse path.

Figure 12 shows the voltage measured on the forward and reverse path detectors at 500MHz with RF_{IN} swept and RF_{OUT} terminated with 50Ω. The vertical separation between these traces relates directly to the directivity of the bridge.

Figure 13 shows the effect of varying the load on the measurement of forward power. Defined power levels are applied to the RF_{IN} input, and the return loss of the load on RF_{OUT} is varied from 0-20dB. As expected, with the return loss in that range, power measurement accuracy is quite good. But, as the return loss is reduced to below 10dB, the power measurement error starts to increase. It is notable that for a return loss of 0dB, the error is still around 1dB.

In Figure 14, the ADL5920 is used to measure the return loss of the load, also at 1GHz. A known return loss is applied to the RF_{OUT} port. V_{RMSF} and V_{RMSR} are measured, and the return loss is back-calculated.

There are several points to note about this plot. First, it shows that the ADL5920's ability to measure return loss degrades as return loss improves, which is due to the directivity of the device. Second, note how measurement accuracy degrades as the drive power drops, which is due to the limited detection range and sensitivity of the ADL5920's on-board rms detectors. The third observation relates to the apparent ripple in the traces. This is caused by the fact that each measurement is being taken at a single return-loss phase. If the measurement was repeated at all return loss phases, a family of curves would result, with vertical width roughly equal to the vertical width of the ripple.

Applications

With the ability to measure inline RF power and return loss, the ADL5920 is useful in multiple applications. Its small size means it can be dropped into many circuits without a significant space impact. Typical applications include in-circuit power monitoring at RF power levels up to 30dBm, where insertion loss is not critical.

The return loss measurement capability is typically used in applications where an RF load is being monitored. This could be a simple circuit to check that an antenna has not been damaged or broken off (that is, catastrophic failure). However, ADL5920 can also be used to measure scalar return loss in materials analysis applications. This is most applicable at frequencies below 2.5GHz where directivity (and thereby measurement accuracy) is greater than 15dB. EW

Cabling and the invisible threat of non-compliance

By Eland Cables development engineers

Since 2010, some 1.1 million homes have been built in England alone, with the overall number of homes rising by 15% in 2017, according to the UK government. In London, Mayor Sadiq Khan plans to invest £250m in buying and preparing land for new and affordable housing.

Growth is not restricted to the residential sector alone. The London Bridge station rebuild was a major focus in the capital, and a glance at the skyline shows a city constantly growing.

Powering all this is a busy construction industry, with a raft of materials and products underpinning every project, one of which

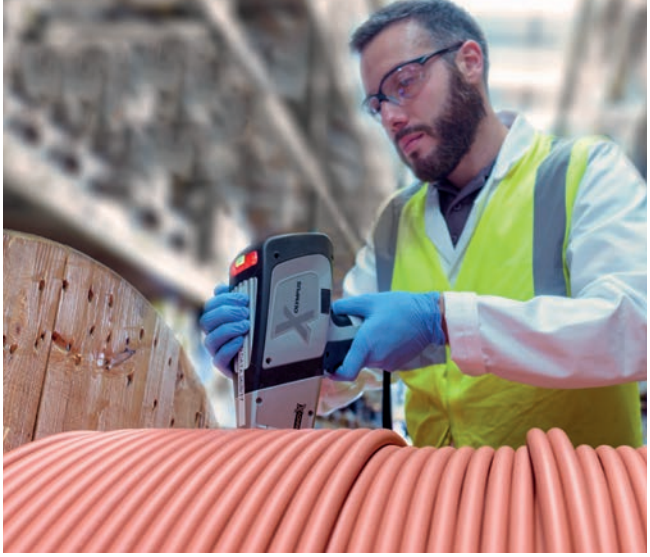

is cabling. The quality of every construction depends among other things on the quality of its cable, hence building firms need to ensure that the materials they use are truly fit for purpose.

There are British, European and international standards that define cable construction and performance, as well as clear rules for compliance.

Standards and Compliance

Various industry bodies are charged with keeping standards up to date and fit for purpose, and the specifications they publish are stringent to safeguard safety and reliability. The UK's national standards body – the BSI (British Standards Institute) – is part of CENELEC (the European Committee for Electrotechnical Standardisation) and is bound as a member to adopt its recommendations on top of the UK regulations, promoting uniformity in standards across the EU.

In July 2017, an EU regulation called Construction Products Regulation (CPR) came into force, which classifies newly-manufactured cables by their reaction to fire. Cables used for fixed installations must be tested for their flame characteristics and classified from A to F, with additional classifications for smoke emissions, flaming droplets and acidity.

However, despite all the regulation and testing, it's still estimated that up to 20% of all cables in circulation in the UK are either sub-standard, counterfeit or non-approved. For a commercial or industrial build, sub-standard cable can result in downtime, reliability issues and ballooning maintenance costs at best and major safety hazards at worst. For residential projects, sub-standard cable can be a dangerous time bomb and for developers a major business risk. As such, non-compliance is a huge threat that jeopardises the industry's ability to deliver.

Part of this big responsibility falls to the site developers and engineers to be vigilant and take a proactive stance. They play a key role in ensuring that only compliant products make it onto site, ready for installation.

Up to Standard

The sheer number cable types and standards can be overwhelming, including cables for power, data, control and instrumentation; low, medium and high voltage; armoured or fire-resistant; and covered in different materials that include PVC and Low Smoke Zero Halogen (LSZH) compounds.

RoHS Directive (the Restriction of Hazardous Substances) is a

well-known and established Europe-wide legislation, designed to keep products that contain substances with potentially devastating impacts on health out of the supply chain. These include lead, mercury and hexavalent chromium, among others. All cables sold inside the EU need to be RoHS-compliant and most are; however, it's essential to be absolutely certain.

In addition, CPR and other standards determine the flame propagation (Vertical Flame Testing to BS EN 60331-1-2) and gas emissions of cables under fire conditions (BS EN 60754). For instance, PVC emits chlorine gas when burnt, which turns into hydrochloric acid when mixed with water from the atmosphere. It also produces a thick, light-obscuring smoke that can damage sensitive equipment and risk the safe evacuation of buildings. This is why Low Smoke Zero Halogen sheath materials are now mandatory for cables in public buildings and spaces in the UK – they emit low levels of toxic fumes, 60% less dense black smoke and no acid gases.

Regulating the Supply Chain

Cable manufacture is now limited in the UK. The bulk of manufacturers of British and European standard cables are based in Italy, Spain, Portugal and Turkey, making it harder to police standards and regulations.

Small changes to the raw materials going into the cable can have a huge bearing on the final product. For example, small reductions in the copper content of the conductor can have a major impact on the performance of the finished product; or the water used to mix with the pellets for the sheathing and insulation materials might have elevated levels of lead as a result of pollutants from an upstream factory.

All of this is manageable and helps prevent sub-standard, non-compliant cable from entering the UK supply chain. Sadly, the rules aren't always enforced to the degree they should be, meaning that in most cases it's not immediately apparent whether the installed cable is non-compliant. It might be years before problems come to light – for instance, it was only recently discovered that 11 million metres of non-compliant low-voltage cable made it onto the UK market in 2010, and only seven million of them were withdrawn. The low copper content of the cables makes them a significant potential fire risk with little knowledge of where that cable had ended up, making retrieval and replacement very difficult.

Holes in the Net

It's not enough to assume something is up to standard just because there hasn't been a reported problem with that product or supplier before. Good manufacturers conduct extensive tests on their cables before releasing them to market. In addition, third-party accreditation markings provide valuable reassurance by indicating the compliance of a tested length, although just against a sample rather than batch-by-batch or at the cable-drum level. There's also the issue of fraudulent cables available for sale – deliberate sub-standard copies made to look the part. It underlines the importance of testing throughout the cable supply chain, not just at the point of manufacture but also before delivery to the end user.

What's a Site Developer To Do?

The worst is to assume. Most projects source their cables from suppliers that amalgamate different types and sizes into a timely delivered order, so going direct is not always an option.

The construction firm and its contractors rely on the cable supplier to be certain that every batch from every manufacturer is compliant and as expected, which requires extensive testing, most likely beyond the in-house capabilities of most suppliers. The end user should be able to assume that any cable bought from a UK manufacturer, supplier or wholesaler is wholly compliant and fit for purpose, although sadly that's not universally the case. Admittedly, no control system is ever perfect.

To help, here are a few steps site engineers and developers can take to minimise the risk of substandard or non-compliant cable:

- **Look into the supplier's supply chain.**
  This information shouldn't be hard to get from the supplier, and it's basic due diligence for any project. It's important the supplier is tracking its products and – ideally – testing them with its own or third-party testing facilities. If this information isn't forthcoming, don't hesitate to walk away.
- **Check for the appropriate markings.**
  Looking at the cable itself is a basic and easy check that is all too often overlooked. It's not failproof; small changes, a testing mistake, or fraudulent behaviour might see a bad cable stamped with all the right markings, but the print legend is the first indicator of whether the cable is what it should be.
  Similarly, does the label have the relevant information including CPR compliance details where appropriate?
- **Check for accreditations.**
  High-quality suppliers will proudly display their ISO, BSI and UKAS accreditations. If the supplier offering the best or cheapest deal doesn't do the same, it's worth wondering why. In addition to these reputable industry accreditations there are also internationally-recognised marks such as the BSI RoHS Trusted Kitemark, which identify organisations that can assure quality and compliance.

If ever a site engineer suspects they have sub-standard cable on their hands, they can have an accredited third party test it, or report it to the proper authorities to do so. An independent assessment into the quality and compliance of the cable will provide certainty and, with a bad batch, a remedial action can be taken; prevention is always better than cure.

Question Suppliers

Construction underpins so much of our everyday lives, including our homes, communities, workplaces and transport systems. Cabling might not be the most visible or glossy part, but it's integral, woven throughout the entire ecosystem, and it's crucial to get right.

What's important to remember is that having an established and successful industry doesn't automatically mean its supply chain is always reliable and trustworthy. Instead, it is up to each firm to question suppliers and ensure that the industry adheres to its own standards and remains compliant. EW

Improved charge balance A/D converter for load cell signal measurements

By Jianhua Tang and Yingqun Hua, Jiangsu University, China

The charge balance analogue-to-digital (A/D) converter is a well-known high accuracy device, widely used in load cell measurement circuits; a load cell is a transducer that outputs an electrical signal with a magnitude directly proportional to the force being measured. However, the traditional charge-balance A/D converter suffers when its input signal is close to the reference, making it unstable. Many are focusing on improving this problem, and here we discuss a design theory of an improved converter for load cell measurement circuits, one that is stable when its input signals are close to the reference.

The improved converter is identical to the traditional version except for one important attribute. Figure 1 shows the improved charge balance technique. The one feature that differs from the traditional converter is that the voltage v_{ramp} is used as a comparator reference. The traditional converter uses a constant voltage of zero as reference, whereas v_{ramp} in the improved converter is a sawtooth waveform; see Figure 2. The slope of the r_{amp} voltage is denoted by m_{ramp}.

In all respects other than the comparator reference voltage, the rules of operation of the improved converter are the same as for the traditional type. In both converters the integrator capacitor is charged and discharged by i_{sig} and I_{ref} during two phases, and the magnitude of the input voltage is determined from the measured lengths of the charge and discharge times. In the improved converter, however, the transition between phases one and two occurs when the falling v_{out} ramp crosses the rising v_{ramp} ramp, rather than when v_{out} reaches zero.

Figure 3 shows a typical conversion cycle. Variables v_i and v_f represent the initial and final values of v_{out} for a single conversion cycle, whereas variable t_x is the length of phase one, with the total length of the conversion cycle being T_0. The value of v_{out} at the transition between phases is denoted by v_x.

The traditional charge-balance A/D converter suffers when its input signal is close to the reference, making it unstable

Stability Analysis

In Figure 3 the slopes of v_{out}, during the two phases are governed by i_{sig} and I_{ref} which combine to form the total current into the capacitor. The two components of the slope of this voltage are identical to those of the traditional converter.

Figure 4 shows the manner in which the slope components m_{sig} and m_{ref} contribute to the slopes of v_{out} during the two phases.

For an arbitrary set of constant slopes m_{sig}, m_{ref} and m_{ramp}, an equation can be obtained that relates the values of v_i and v_f:

$$v_f = v_i\left(1 - \frac{m_{ref}}{m_{sig} + m_{ref} - m_{ramp}}\right) + T_0 m_{sig} \qquad (1)$$

Equation 1 gives the value of v_{out} at the end of a conversion period in terms of its value at the beginning of the period, when the input signal is constant. This equation may be used recursively to generate a sequence of peaks in v_{out} that would result from an arbitrary initial value. The recursion may be written in the simpler form:

$$v(k+1) = bv(k) + c, \quad k = 0,1,2,\ldots \qquad (2)$$

The values of the peaks of v_{out} are represented by v(k), and the constants b and c correspond to the following terms from Equation 1:

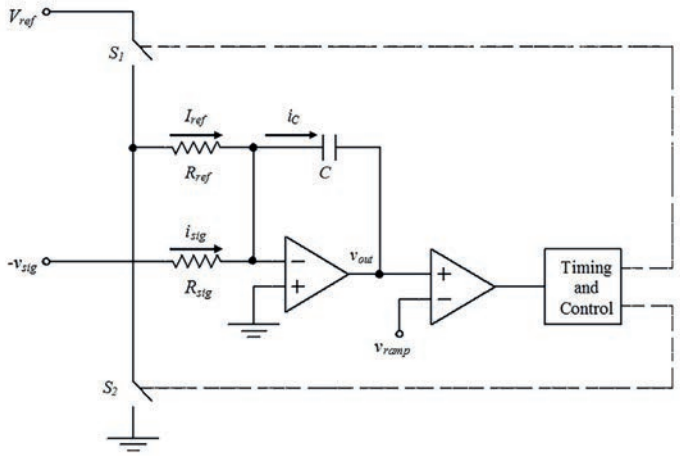

Figure 1: Schematic diagram of an improved charge balance A/D converter

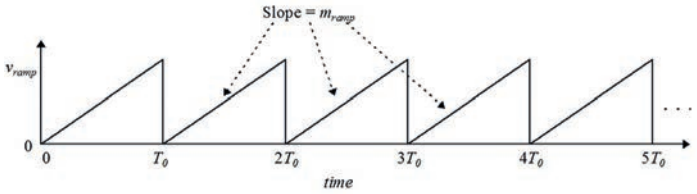

Figure 2: Plot of the sawtooth voltage used as comparator reference

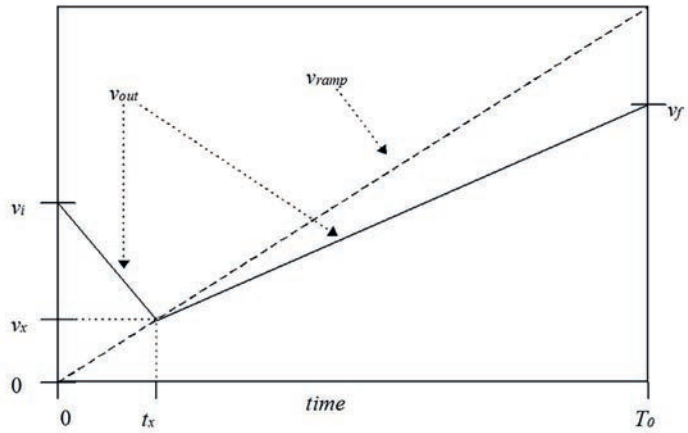

Figure 3: Integrator output voltage during a typical conversion cycle

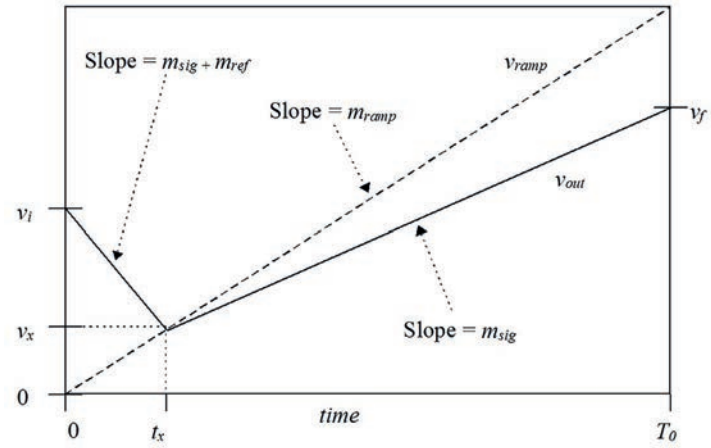

Figure 4: Illustration of the slopes of vout during a typical conversion cycle

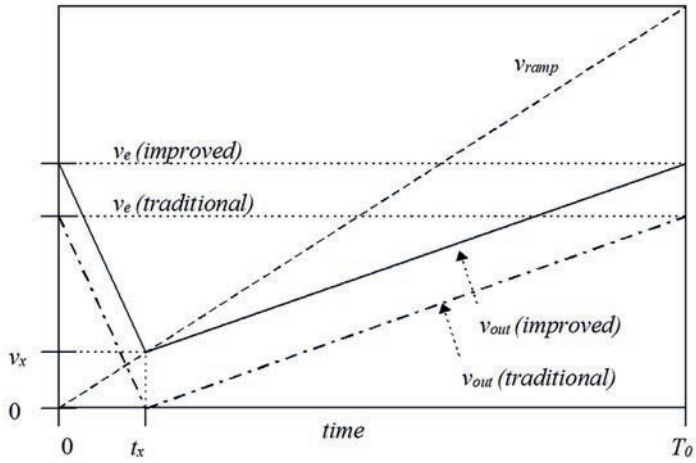

Figure 5: Comparison of conversion cycles for the traditional and the improved converter

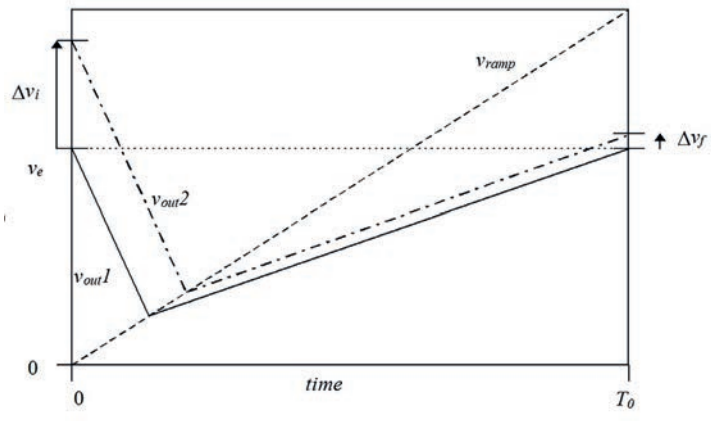

Figure 6: Conversion cycles with a ramp slope greater than the signal slope

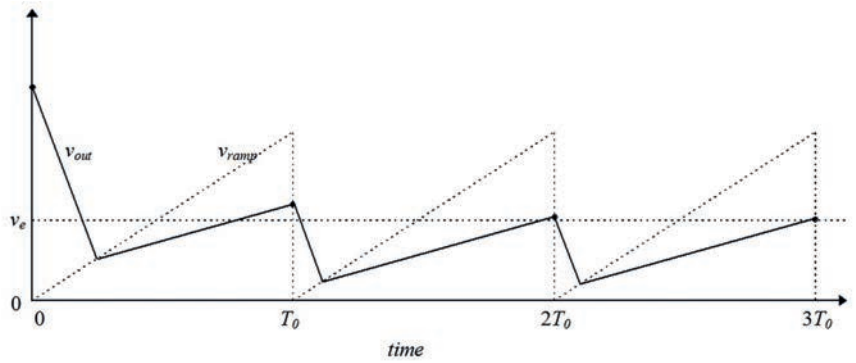

Figure 7: Typical convergence with a ramp slope greater than the signal slope

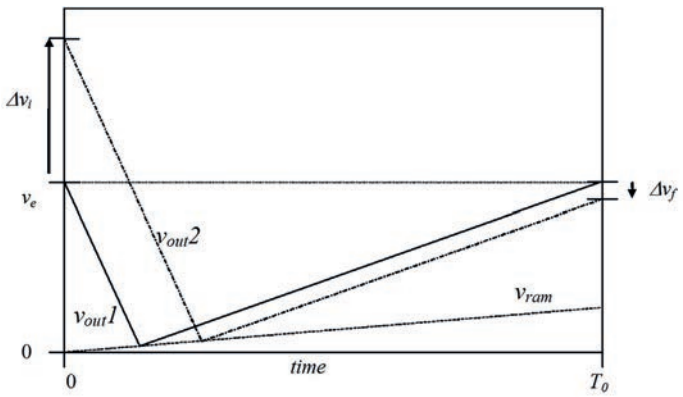

Figure 8: Conversion cycles with a signal slope greater than the ramp slope

$$b = 1 - \frac{m_{ref}}{m_{sig} + m_{ref} - m_{ramp}} \quad (3)$$

$$c = T_0 m_{sig} \quad (4)$$

Figure 5 is a plot of v_{out} during equilibrium for a hypothetical set of parameters, for both the traditional and improved converters. The figure shows that the equilibrium peak voltage of the improved converter is greater than that of the traditional converter for the same input signal. In fact, function v_{out} for the improved converter is greater than v_{out} in the traditional converter by a constant difference v_x over the entire conversion period. This is a consequence of the equality of the corresponding slopes of v_{out} for the two converters.

Each converter uses the same reference current, which determines the reference slope m_{ref}. For this example, the input current i_{sig}, which determines the slope m_{sig}, is also identical for the two converters. In Figure 5, although the integrator output voltage is greater for the improved converter,

The improved converter can measure higher input currents than the traditional converter, without becoming unstable

the transition time between the two phases, t_x, is the same for both converters.

Because of the recursive manner in which peaks of v_{out} are produced by the improved converter, there are certain conditions when the converter is not stable. Successive evaluation of Equation 2 using an arbitrary initial value v(0) yields the following equation:

$$\begin{aligned} v(1) &= b \cdot v(0) + c \\ v(2) &= b^2 v(0) + bc + c \\ &\vdots \\ v(N) &= b^N v(0) + b^{N-1}c + b^{N-2}c + \ldots + b^2 c + bc + c \\ \Rightarrow v(N) &= b^N v(0) + c\sum_{n=0}^{N-1} b^n \end{aligned} \quad (5)$$

Equation 5 is an expression for the peak v_{out} after N conversion cycles, given a constant input voltage, and a value of v(0) for v_{out} at the start of the first cycle. For both converters, the condition must hold for stable sequences: v(N) is always finite even though N is infinite.

Equation 5 shows that they converge uniformly to finite limits if and only if $|b| < 1$. The following alternate expression of the condition for stability is obtained by substituting Equation 3 into $|b| < 1$ to help determine the inequality for the stability condition:

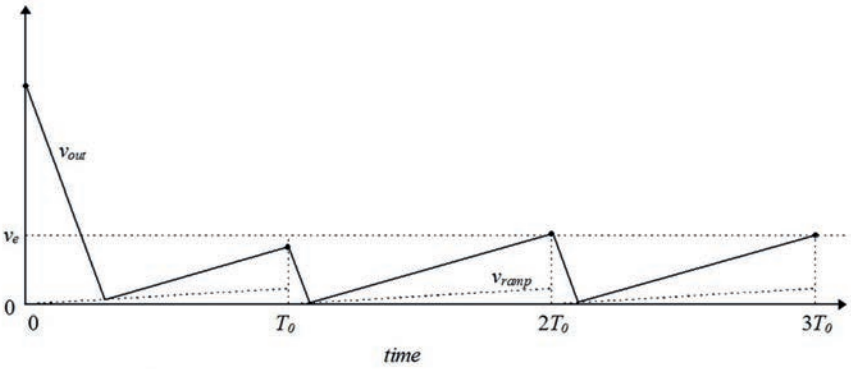

Figure 9: Typical convergence with a signal slope greater than the ramp slope

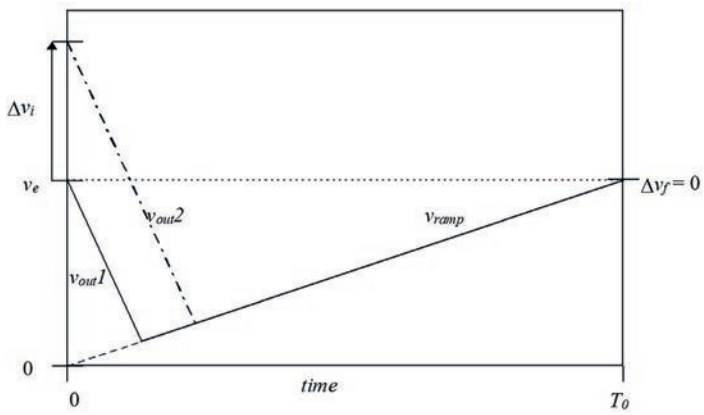

Figure 10: Conversion cycles when the signal and ramp slopes are equal

$$m_{sig} < m_{ramp} - \frac{1}{2} m_{ref} \quad (6)$$

The same procedure can determine the corresponding stability condition for a traditional converter, given:

$$m_{sig} < -\frac{1}{2} m_{ref} \quad (7)$$

where m_{ref} is negative.

The inequalities of Equations 6 and 7 differ only in the m_{ramp} term that appears in the equation for the improved converter. The stability constraint of Equation 7 requires that the input signal current i_{sig} be less than half the magnitude of the reference current I_{ref} for the traditional converter. However, the presence of the m_{ramp} term in Equation 6 raises the limit of the allowable input signal current for the improved converter. Thus, the improved converter can measure higher input currents than the traditional converter, without becoming unstable.

The values of m_{ramp} and m_{sig} can affect the convergence of the converter because they influence the value of the coefficient b of Equation 3 that is used in the difference Equation 2. Parameter b of Equation 3 may be positive, negative or zero when m_{ramp} and m_{sig} change: if b is not zero, its sign determines whether v_{out} overshoots the equilibrium value with each iteration. When $m_{ramp} > m_{sig}$ then b is positive and there's no overshoot; see Figure 6.

Figure 6 shows two different v_{out} curves, v_{out1} at equilibrium and v_{out2} converging to equilibrium. Both the initial and final values of v_{out1} equal the equilibrium peak value, v_e. The initial value of v_{out2} is greater than the equilibrium value by the amount Δv_i. The peak value of v_{out2} at the end of the conversion period is also greater than the equilibrium value by the amount Δv_f. The magnitude of Δv_f is smaller than that of Δv_i because the system is stable. Moreover, the sign of Δv_i is the same as that of Δv_f, indicating that v_{out2} does not overshoot the equilibrium value in this example. This is a consequence of the positive sign of b and the fact that the ramp slope exceeds the signal slope. The sequence of peaks of v_{out} converges to the equilibrium value from above here. Figure 7 shows this process for several successive conversion periods.

When the signal slope exceeds the ramp slope and b is negative, the peak value of v_{out} overshoots the equilibrium value with each conversion cycle. This condition is shown in Figure 8.

Two different v_{out} curves are shown again, v_{out1} at equilibrium and v_{out2} converging to equilibrium. The initial value of v_{out2} again exceeds the equilibrium value by Δ_{vi}, and the peak value of v_{out2} at the end of the conversion period differs from the equilibrium value by Δv_f.

As in Figure 6, the magnitude of Δv_f is smaller than Δv_i, but the sign of Δv_i is negative, indicating that v_{out2} overshoots the equilibrium value. This occurs because the ramp slope is smaller than the signal slope, causing b to be negative.

The sequence of peaks of v_{out} converges to the equilibrium value in an oscillatory manner in this example. Figure 9 shows this behaviour for a few conversion periods.

If the signal and ramp slopes are equal, b is zero and there is no overshoot or undershoot. Convergence to equilibrium occurs in only one conversion period, as shown in Figure 10. When b is zero, the sequence of converter output peaks converges to c after the first iteration of the difference equation, regardless of the past values of the output or input, which indicates that the equilibrium voltage $v_e = c$ in this case. EW

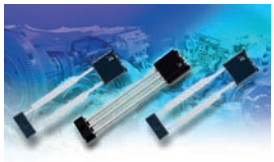

Allegro launches most advanced transmission speed sensor ICs

Allegro MicroSystems Europe has released its most-advanced transmission speed sensor family members, complete with ASIL B certification. The A19520, A19530 and A19570 magnetic sensor ICs measure speed and direction information and integrate EMC protection capacitors. The sensors also incorporate Allegro's SolidSpeed Digital Architecture, a mixed-signal architecture that enables the widest dynamic range of air gap, distinction of vibration versus rotation, stray field immunity and highly adaptive performance. The A19520 uses Hall effect technology and a two-wire interface. The A19530 provides advanced signal processing, open/short detection capability and selectable speed or speed and direction output protocols. It uses Hall effect and a three-wire interface. Using GMR and a two-wire interface, the A19570 brings the same high algorithmic performance as its Hall-effect counterparts, but at significantly larger air gaps and with flexible device orientations.

www.allegromicro.com

Siglent Technologies presents a new flagship oscilloscope

Siglent Technologies launched its new, flagship oscilloscope series – the SDS5000X, available with bandwidths of 350, 500 and 1GHz, and featuring a maximum sample rate of 5GS/s, 250Mpts acquisition memory and a waveform-update rate of up to 110,000wfm/s. To help maintain high test speeds, many of its waveform analysis features are implemented in hardware.

The SDS5X includes a full digital trigger with qualified and zone triggering to help isolate faults more quickly. This technique enables a highly-sensitive and accurate trigger control. It also includes a new low-noise front-end that delivers a vertical sensitivity of 500µV/div, making the SDS5X a perfect tool for debugging small signals.

The scope includes a large 10.1" touchscreen that includes gesture operation and a clear layout that makes the scope extremely easy-to-use.

www.siglenteu.com

Mouser now shipping TI's DRV835x smart gate drivers

Mouser Electronics is now stocking the DRV835x three-phase smart gate drivers from Texas Instruments (TI). These highly-integrated gate drivers are designed for three-phase brushless DC (BLDC) motor applications, including field-oriented control (FOC), sinusoidal current control and trapezoidal current control. These drivers use smart gate drive (SGD) architecture to decrease the number of external components typically necessary for MOSFET slew rate control and protection circuits. The SGD architecture also optimises dead time to prevent shoot-through conditions, provides flexibility in decreasing electromagnetic interference (EMI) by MOSFET slew rate control, and protects against gate short circuit conditions through VGS monitors. The drivers provide optional integrated current shunt amplifiers to support different motor control schemes and a buck regulator to power the gate driver or external controller. A strong gate pulldown circuit helps prevent unwanted dv/dt parasitic gate turn on events.

www.mouser.com

Powertip development board for Cortex-M4 processor applications

Inelco Hunter now offers a Powertip development board for Cortex-M4 processor applications where a display screen interface is required. The board is tailor-made for Cortex-M4 STM32F429IGT6 processors.

The development board features a built-in 22-pin GPIO interface that's compatible with Powertip 4 in 1 series TFT 3.5", 4.3", 5" and 7" displays. The board also supports any display with a resolution of up to RGB 1024 x 768 using the same industry-standard GPIO interface.

There are twelve Powertip 4 in 1 series displays that are compatible with the development board, some with CTP/RTP touch options: TFT only, TFT plus resistive touch panel, TFT plus OGS PCAP, TFT plus GG PCAP, and TFT plus borderless GG PCAP.

Specifications for the board include a 180MHz Cortex-M4 STM32F429IGT6 processor, 8MB SDRAM, 16MB SPI Flash, and 1x Micro SD (under 32G).

www.inelcohunter.co.uk

5V 60A DC-DC converter accepts a 200 to 425V input

TDK Corporation (TSE 6762) introduced the TDK-Lambda brand PH300A280-5 DC-DC converter, completing the PH-A280 series of 200 to 425V input 50-300W power modules. The new model is designed for data communications and renewable energy applications utilising 380V HVDC (High Voltage DC).

The new model is rated at 5V 60A and has a wide 2.5-6V adjustment range to accommodate non-standard voltages. Packaged in the industry standard half-brick format (61.0 x 12.7 x 57.9mm), it has efficiency of 89% and can operate at full load with -40°C to +100°C baseplate temperatures. The converter can be conduction cooled, making it suitable for use in sealed outdoor enclosures, liquid cooled applications or convection cooled with an optional heatsink.

All PH-A280 modules include a five-year warranty. The series is fully isolated to 3,000Vac and safety certified to IEC/EN 60950-1.

www.uk.tdk-lambda.com

Cost-effective, high-accuracy PXI RTD simulator modules

Pickering Interfaces now offers a 40-263 PXI RTD simulator module range that provides a cost-effective method of simulating PT100, PT500 or PT1000 RTDs (resistance temperature detectors) with high accuracy. The range supports 4, 8, 12, 16, 20 or 24 channels in one or two PXI slots with channels able to be set as short or open circuit to simulate faulty wiring to a sensor.

The modules are available with resistance ranges of 40-900Ω for PT100 simulation, 200-4500Ω for PT500 simulation and 400-9000Ω for PT1000 simulation. All versions are suitable for simulating a temperature range of -150°C to over +850°C for their given sensor type. The use of resistance value calls makes programming simple.

The 40-263 range provides a convenient system for verifying channel resistance using an external DMM connected to the calibration port.

www.pickeringtest.com

PROTEUS DESIGN SUITE

Advanced PCB features for professional board design

DESIGN ROOMS

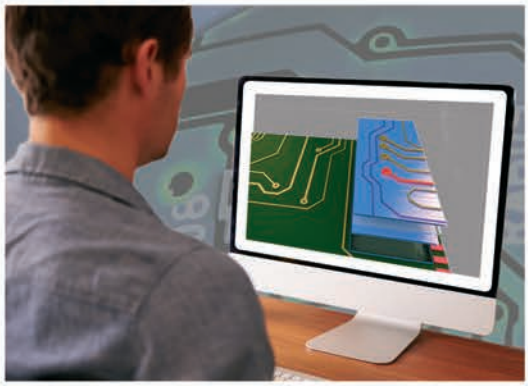

Set design rules that apply in user specified areas of the PCB.

LAYER STACKUP

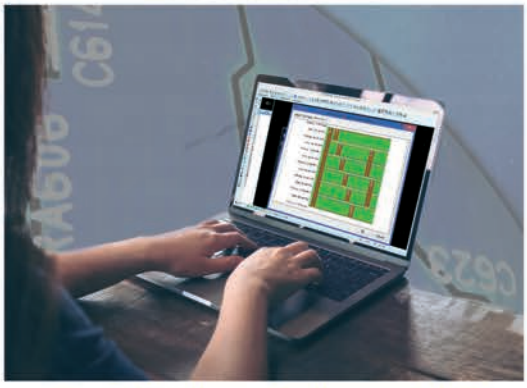

Control the layer stackup and drill ranges for smarter routing.

SERPENTINE ROUTING

Easily length match tracks against each other or to a target distance.

DESIGN VARIANTS

Edit the fitted status of parts or re-place with pin compatible alternatives.

The Proteus Design Suite provides advanced features at an affordable price. Try it today!

Visit: www.labcenter.com

Tel: +44 (0) 1756753440
E-Mail: info@labcenter.com
youtube.com/c/LabcenterElectronicsLtd

Labcenter Electronics www.labcenter.com

Get your TI Chips at Mouser

Mouser is an authorised distributor with the largest selection of Texas Instruments' chips in stock

mouser.com/ti

MOUSER ELECTRONICS